

Lagrangian Overturning Pathways in the Eastern Subpolar North Atlantic

Oliver J. Tooth,^a Helen L. Johnson,^a Chris Wilson,^b

^a *Department of Earth Sciences, University of Oxford, Oxford, United Kingdom*

^b *National Oceanography Centre, Liverpool, United Kingdom*

Corresponding author: Oliver J. Tooth, oliver.tooth@seh.ox.ac.uk

6 ABSTRACT: The strength of the Atlantic Meridional Overturning Circulation (AMOC) at sub-
7 polar latitudes is dominated by water mass transformation in the eastern Subpolar North Atlantic
8 (SPNA). However, the distribution of this overturning across the individual circulation pathways of
9 both the Subpolar Gyre (SPG) and the Nordic seas overflows remains poorly understood. Here, we
10 introduce a novel Lagrangian measure of the density-space overturning to quantify the principal
11 pathways of the time-mean overturning circulation within an eddy-permitting ocean model hind-
12 cast. By tracing the trajectories of water parcels initialised from the northward inflows across the
13 OSNAP East section, we show that water mass transformation along the pathways of the eastern
14 SPG accounts for 55% of the mean strength of the eastern subpolar AMOC. Water parcels fol-
15 lowing the dominant SPG pathway, sourced from the Sub-Arctic Front, form upper North Atlantic
16 Deep Water by circulating horizontally across sloping isopycnals in less than 2 years. A slower
17 SPG route, entrained by overflow waters south of the Iceland-Faroes Ridge, is a crucial conduit
18 for subtropical-origin water masses to penetrate the deep ocean on subdecadal timescales. On re-
19 producing our findings using time-averaged velocity and hydrographic fields, we further show that
20 the Nordic seas overflow pathways integrate multiple decades of water mass transformation before
21 returning across the Greenland-Scotland Ridge. We propose that the strong disparity between the
22 overturning timescales of the SPG (interannual) and the Nordic seas overflows (multi-decadal)
23 has important implications for the propagation of density anomalies within the eastern SPNA and
24 hence the sources of AMOC variability.

25 1. Introduction

26 The Subpolar North Atlantic (SPNA) Ocean is a critical component of the global climate sys-
27 tem. Here, light subtropical waters, conveyed in the upper 1000 m, are transformed by intense
28 surface buoyancy loss into dense North Atlantic Deep Water (NADW) that feeds the lower limb of
29 the Atlantic Meridional Overturning Circulation (AMOC). As the principal northern hemisphere
30 conduit for the exchange of heat and anthropogenic carbon between the atmosphere and the deep
31 ocean, the strength of the AMOC has profound implications for Arctic sea ice (Yeager et al. 2015),
32 North Atlantic sea level (McCarthy et al. 2015), and European climate (Jackson et al. 2015).

33 The large-scale circulation of the SPNA is characterised by the complex interplay between the
34 3-dimensional circulations of the Subpolar Gyre (SPG) and Nordic seas overflows. Isopycnals
35 shoal strongly with distance westwards across the basin, such that the strength of the AMOC
36 is more appropriately measured by the transformation from lighter to denser waters (i.e., an
37 overturning in density-space), rather than in traditional depth-space (Mercier et al. 2015; Li et al.
38 2017). Historically, climate modelling studies identified deep water formation in the Labrador
39 Sea interior as a major contributor to AMOC variability (Danabasoglu et al. 2014; Menary et al.
40 2015; Li and Lozier 2018). However, recent observations made by the Overturning in the Subpolar
41 North Atlantic Program (OSNAP) show that water mass transformation east of Greenland (north
42 of OSNAP East, see Fig.1) dominates both the mean strength and variability of the subpolar
43 AMOC on interannual timescales (Lozier et al. 2019; Li et al. 2021). Therefore, understanding the
44 overturning dynamics of the eastern SPNA, including identifying potential teleconnections, is of
45 increasing importance.

46 The eastern SPNA is fed from the south by the North Atlantic Current (NAC), which incorporates
47 both the upper limb of the AMOC and the southernmost limb of the cyclonic SPG (Fig. 1a).
48 North of OSNAP East, the NAC distributes Subpolar Mode Waters (SPMWs) of nearly uniform
49 temperature and salinity (McCartney and Talley 1982) between the eastern SPG (12.7 Sv where
50 $1 \text{ Sv} \equiv 10^6 \text{ m}^3 \text{ s}^{-1}$) and the Atlantic inflows to the Nordic seas (8.4 Sv) (Sarafanov et al. 2012),
51 which in-turn supply approximately equal volumes of NADW to the lower limb of the AMOC
52 (Chafik and Rossby 2019; Petit et al. 2020). In the eastern SPG, SPMWs circulate cyclonically
53 around the Iceland Basin, undergoing continuous densification (Brambilla and Talley 2008) owing
54 to intense surface buoyancy loss (Petit et al. 2020). On crossing the Reykjanes Ridge, weakly

55 stratified SPMWs are said to be "pre-conditioned" (Thierry et al. 2008; de Boissésou et al. 2012)
56 to form upper NADW downstream through convection on the edge of the EGC (Le Bras et al.
57 2020). This transformation along the horizontal boundary currents of the eastern SPG has been
58 characterised as a form of "lateral subduction" by Chafik and Rossby (2019), and is estimated to be
59 responsible for more than 40% of overturning in density-space at OSNAP East (Zhang and Thomas
60 2021). Away from the SPG boundaries, upper NADW with a similar composition to Labrador Sea
61 Water (Pickart et al. 2003) is also formed by deep convection in the Irminger Sea interior (de Jong
62 et al. 2012; Piron et al. 2016). Collectively, these two modes of dense water formation dominate
63 the variability of the subpolar AMOC on interannual (Petit et al. 2020) and decadal (Desbruyères
64 et al. 2019) timescales. Although the processes governing water mass transformation in the eastern
65 SPNA have been subject to extensive research (e.g., Grist et al. 2009, 2016; Desbruyères et al.
66 2019; Petit et al. 2020, 2021), we have yet to establish the distribution of density-space overturning
67 across the branches of the NAC.

68 Conversely, the transport of waters overflowing the Greenland-Scotland Ridge shows little vari-
69 ability on decadal timescales (Østerhus et al. 2019). The freshest, densest variety of overflow
70 water, Denmark Strait Overflow Water (DSOW), overflows the Denmark Strait sill west of Iceland
71 before entraining ambient Atlantic water to form lower NADW in the Deep Western Boundary
72 Current (DWBC) (Dickson and Brown 1994; Dickson et al. 2008; Jochumsen et al. 2012). To the
73 east, Iceland Scotland Overflow Water (ISOW) descends from the Norwegian Sea into the Iceland
74 Basin (Østerhus et al. 2008), where entrainment of SPMW produces its characteristic high salinity,
75 observed downstream (Yashayaev and Dickson 2008). ISOW subsequently flows southward at
76 depth along the eastern flank of the Reykjanes Ridge (Lankhorst and Zenk 2006), where it is
77 partitioned between the cyclonic DWBC (Bower and Furey 2017) and interior pathways flanking
78 the Mid-Atlantic Ridge (Zou et al. 2020a). Diagnosing the contribution of these deep pathways to
79 the density-space overturning measured at OSNAP East represents a critical next step in advancing
80 our understanding of the subpolar AMOC.

81 The overturning circulation of the SPNA has been studied from both Eulerian and Lagrangian per-
82 spectives. The Eulerian perspective, typified by trans-basin hydrographic sections (e.g., Greenland-
83 Portugal OVIDE section), derives understanding from integrated AMOC metrics which quantify
84 the total water mass transformation occurring at the basin scale (Lherminier et al. 2007; Lozier

et al. 2019). In contrast, the Lagrangian perspective seeks to characterise the spatial and temporal evolution of the individual circulation pathways comprising the subpolar AMOC (Bower et al. 2019). This Eulerian-Lagrangian duality is best demonstrated by OSNAP itself, since the program simultaneously employs a trans-basin observing system (Lozier et al. 2017; Li et al. 2017) to quantify the state of overturning, and subsurface floats to trace the deep pathways of the overflows (Zou et al. 2020a). However, what remains unaddressed is how the Lagrangian circulation pathways relate to the Eulerian integrated measures of overturning evaluated by ocean mooring arrays. In the eastern SPNA, this means quantifying how the overturning measured at OSNAP East is distributed amongst the pathways of the SPG and the Nordic seas overflows. Moreover, given that recent observations suggest that variation in NADW properties can imprint onto both seasonal and interannual overturning variability (Le Bras et al. 2020), there is a growing need to identify the dominant advective timescales over which density anomalies can propagate within the eastern SPNA.

In this study, we employ Lagrangian particle tracking to investigate the structure of the time-mean overturning circulation in the eastern SPNA within an eddy-permitting ocean sea-ice hindcast simulation. We first establish the fidelity of the gyre and overturning circulations simulated in ORCA025-GJM189 through comparison with observations of the SPNA. By extending the methodology of Georgiou et al. (2020, 2021), we then formalise the concept of the Lagrangian density-space overturning and show how trajectories traced from the northward inflows across a model-defined OSNAP East array reveal the mean pathways of the circulation, including their overturning components. In contrast to traditional integrated metrics, we demonstrate how the Lagrangian density-space overturning can be decomposed to quantify the contributions made by individual pathways to overturning at OSNAP East, their associated advective timescales and the extent of water mass transformation in the Iceland-Rockall and Irminger Basins.

The study is organised as follows. In Section 2, we introduce the eddy-permitting model simulation and Lagrangian particle tracking experiments. Section 3 explores the composition of the time-mean northward transport across OSNAP East. The time-mean Lagrangian overturning in the eastern SPG is defined in density-space in Section 4. In Section 5, we decompose the Lagrangian overturning in the eastern SPG by circulation pathway, quantifying the extent of water mass transformation in each basin and identifying the dominant advective timescales over which

115 overturning takes place. Finally, in Section 6, we reproduce our findings using time-averaged
116 velocity and hydrographic fields, before extending our analysis to investigate the overturning
117 pathways and advective timescales of the Nordic seas overflows. The study concludes with a
118 summary of our principal findings and a discussion of their wider implications for high-latitude
119 AMOC variability (Section 7).

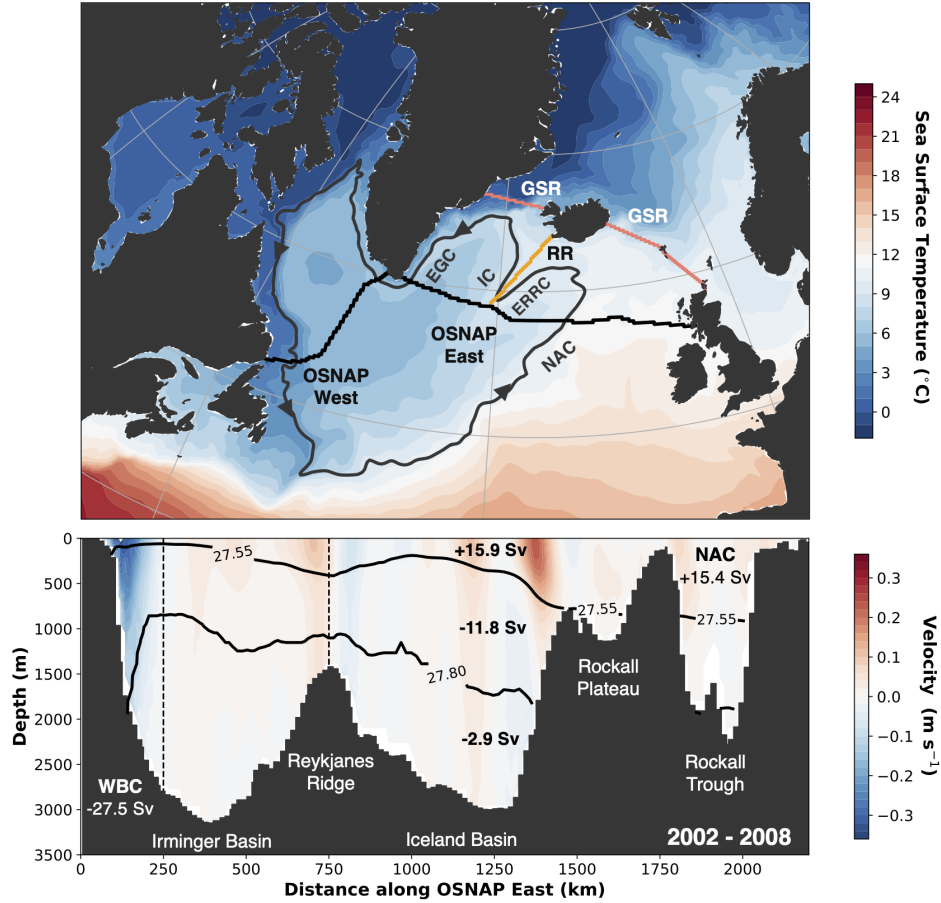


FIG. 1. Time-mean sea surface temperature and volume transports in the SPNA in ORCA025-GJM189. a) The location of the OSNAP observing array superimposed on a map of mean (1976-2015) sea surface temperature and the boundary of the subpolar gyre (defined as the largest closed contour of sea surface height following Foukal and Lozier 2018). The Reykjanes Ridge (RR, orange line) and the Greenland-Scotland Ridge (GSR, pink line) sections are used to define circulation pathways and determine the extent of water mass transformation in each of the subpolar basins in Section 5. The major currents intercepted by the OSNAP East array are identified: North Atlantic Current (NAC), East Reykjanes Ridge Current (ERRC), Irminger Current (IC), and East Greenland Current (EGC). b) Model-derived summertime mean (JJA; 2002-2008) velocity perpendicular to OSNAP East (positive transports are northward) overlaid by $\sigma = 27.55$ kg m⁻³ (the isopycnal of maximum overturning reported by Sarafanov et al. 2012) and $\sigma = 27.80$ kg m⁻³ (the observed upper limit of overflow waters transformed in the Nordic seas). Simulated net transports (bold) are included for the upper layer (< 27.55 kg m⁻³), intermediate layer ($27.55 \leq \sigma < 27.80$) and the deep layer (≥ 27.80 kg m⁻³) following Sarafanov et al. (2012). The NAC transport is defined as the net upper layer transport east of Reykjanes Ridge (dashed line at 750 km). The western boundary current (WBC) transport is defined as the net top-to-bottom transport within 250km of Greenland (dashed line).

2. Methods

a. Model description

To investigate the nature of the time-mean overturning circulation in the eastern SPNA, we use output from the ORCA025-GJM189 ocean sea-ice hindcast simulation configured during the Drakkar project (Barnier et al. 2006). The simulation uses the ORCA025 global configuration of the Nucleus for European Modelling of the Ocean (NEMO) model (Madec 2014), coupled to the thermodynamic Louvain-la-Neuve Ice Model version 2 (LIM2) (Fichefet and Morales Maqueda 1999). The model is implemented on a tripolar quasi-isotropic grid with a nominal horizontal resolution of $1/4^\circ$ (27.75 km at the equator, 13.8 km at 60°N) and 75 unevenly spaced z-partial-step-coordinate levels, ranging from 1 m at the surface to 200 m below 4000 m depth. While there is no explicit parameterisation of mesoscale eddy mixing in this simulation, sub-grid scale diffusion of momentum and tracers does admit the partial resolution of mesoscale eddies. Full details of the parameterisations included in this ORCA025 configuration can be found in Molines (2021).

The historical atmospheric forcing which drives this hindcast simulation is provided by the Drakkar Forcing Set 5.2 (Dussin et al. 2016). Surface fields in this forcing set, derived from a combination of ERA40 (Uppala et al. 2005) and ERA-Interim reanalyses (Dee et al. 2011), are used to compute the surface heat, freshwater, and momentum fluxes via the CORE bulk formulae (Large et al. 1994). Once initialised from rest using a combination of the Levitus climatological hydrography (Levitus et al. 1998) and Polar Science Center Hydrographic Climatology (Steele et al. 2001), the model simulates the period from 1958 to 2015. In the absence of a dedicated spinup period, we discard the first 18 years of the simulation to allow for the initial adjustment of the model. The depth of the surface mixed layer (MLD) is diagnosed using a potential density criterion, as in MacGilchrist et al. (2020): $\Delta\sigma = 0.01 \text{ kg m}^{-3}$, where $\Delta\sigma$ is the difference in potential density from the sea surface. We additionally construct stationary velocity and hydrographic fields (see Section 6) by averaging 5-day mean model outputs from 1976-2015. To preserve the spatial distribution of wintertime convection when calculating the time-mean MLDs, we elect to average the 5-day mean MLDs between 1976-2015 rather than compute them directly from the time-mean potential density field.

164 We choose to place the simulated period (1976-2015) into context throughout the study by
 165 comparing transports and hydrography along the model's OSNAP East section (defined as in
 166 Menary et al. 2020) with relevant observations. In agreement with previous Lagrangian studies
 167 using models based on ORCA025 (e.g., de Boissésion et al. 2012; Desbruyères et al. 2013, 2015;
 168 MacGilchrist et al. 2020; Asbjørnsen et al. 2021), we will show that the velocity and hydrographic
 169 fields of the ORCA025-GJM189 simulation can adequately reproduce the gyre and overturning
 170 circulations of the eastern SPNA. To provide an initial impression of the model, Figure 1b presents
 171 the summertime mean velocity fields and volume transports across the OSNAP East section during
 172 the 2002-2008 observational period of Sarafanov et al. (2012). Upper ocean transports across the
 173 section are generally well represented within the simulation: the net transport above the 27.55
 174 kg m^{-3} isopycnal between the Reykjanes Ridge and Scotland is 15.4 Sv in the model compared
 175 with 15.5 ± 0.8 Sv observed by Sarafanov et al. (2012) at 59.5°N . Although the simulated top-to-
 176 bottom transport of the Irminger Basin Western Boundary Current (WBC) is 4.6 Sv weaker than
 177 observations during the summers of 2002-2008, we note the strong agreement between the mean
 178 WBC transport (31.0 Sv) in the model and the 32.0 ± 2.7 Sv reported in Sarafanov et al. (2012)
 179 for the extended period between 1978-2006. We also highlight the small simulated deep-water
 180 transport ($\geq 27.8 \text{ kg m}^{-3}$) across OSNAP East (2.9 Sv) compared with the 13.3 ± 1.3 Sv observed
 181 at 59.5°N (Sarafanov et al. 2012). This absence of the densest water masses results from the
 182 excessive entrainment of ambient Atlantic water by the Nordic seas overflows in this simulation
 183 (MacGilchrist et al. 2020), which is a well-documented bias in current-generation ocean circulation
 184 models (e.g., Danabasoglu et al. 2010; Wang et al. 2015).

185 *b. Lagrangian particle tracking*

186 We use the Lagrangian offline particle tracking tool TRACMASS (v7.1, Aldama-Campino et al.
 187 2020) to determine the trajectories of particles advected by the time-evolving ORCA025-GJM189
 188 velocity field. TRACMASS solves the trajectory path through each model grid cell analytically
 189 by assuming that each component of the 3-dimensional velocity field is a linear function of its
 190 corresponding direction (i.e., $u = u(x)$; Blanke and Raynaud 1997). We evaluate particle trajectories
 191 using the regular stepwise-stationary scheme, which linearly interpolates the model velocities
 192 between successive 5-day mean velocity fields using a series of intermediate time steps (Döös

et al. 2017). By assuming that the resulting velocity field remains stationary during intermediate time steps, an exact solution of the resulting differential equations can be found, representing the streamlines within each grid cell (Döös 1995). An important property of all TRACMASS trajectory schemes is their ability to conserve mass and therefore, for incompressible models like NEMO, ensure that the volume transport carried by each particle is conserved along its trajectory (Döös et al. 2017).

We consider purely advective trajectories except in the surface mixed layer. To reconcile the strongly time-dependent process of vertical turbulent mixing with our use of 5-day mean velocity and hydrographic fields, we choose to implement the mixed layer physics scheme of Paris et al. (2013). This ensures that otherwise smooth, advective trajectories adequately sample the effects of vertical turbulent mixing captured in the Eulerian tracer fields. At each time-step, the parameterisation identifies the particles located within the surface mixed layer and introduces a random vertical displacement governed by a maximum vertical velocity of $|w| = 10 \text{ cm s}^{-1}$ (Van Sebille et al. 2013; Georgiou et al. 2021). Unlike alternative diffusive mixing schemes (e.g., Döös 1995), this scheme does not allow particles to be displaced across the base of the mixed layer and hence artificially contribute to dense water formation.

We perform two Lagrangian experiments to determine the structure of the time-mean subpolar AMOC at OSNAP East. In our primary Lagrangian experiment, numerical particles are initialised on the first available day of each month (based on where the centre of the nearest 5-day mean window falls) between 1976-2008 and advected forward-in-time for a maximum of 7 years. In total, more than 11.2 million particles are initialised on the northward inflows across OSNAP East over 396 months, such that the number of particles released scales with the volume transport through each grid cell. A maximum particle transport of 2.5 mSv is chosen to generate sufficiently large monthly ensembles of numerical particles to calculate robust Lagrangian diagnostics (Jones et al. 2016). Following initialisation, particles are advected through the time-evolving velocity field until they return to the OSNAP East section, reach the Greenland-Scotland Ridge (see Fig 1a), or until the 7 year advection time is reached. Our choice of a 7-year maximum particle advection time ensures that >99.1% of particles are intercepted at either OSNAP East or the Greenland-Scotland Ridge. We note that the remaining particles (0.9%), terminated between OSNAP East and the Greenland-Scotland Ridge, overwhelmingly circulate at depth within the lower limb of the AMOC

and thus would contribute negligibly to the time-mean overturning measured at the section. The decision to terminate particles on reaching the Greenland-Scotland Ridge was motivated by the results of a preliminary experiment, which highlighted that inflows to the Nordic seas typically required multiple decades to return to OSNAP East in the form of dense overflow waters. Given that the ORCA025-GJM189 hindcast only simulates a 40 year historical period (1976-2015), we choose to use our primary Lagrangian experiment to investigate the structure of the time-mean overturning within the eastern SPG, south of the Greenland-Scotland Ridge.

In our second, complimentary Lagrangian experiment, we extend our analysis to examine the contributions of both the eastern SPG and the Nordic seas overflows to the time-mean overturning at OSNAP East. To do this, we replicate our primary experiment using stationary velocity and hydrographic fields (1976-2015), whilst also significantly increasing the maximum particle advection time to 60 years in order to explicitly resolve the pathways of the Nordic seas overflows. Moreover, since the stationary velocity field does not evolve through time, we require only a single initialisation of 22,657 numerical particles to sample the entire northward transport across the OSNAP East section. We note that fewer particles are released in our second Lagrangian experiment compared with the average monthly initialisation (28,372) using time-evolving fields since eddy-induced northward transports are substantially weaker across OSNAP East in the stationary velocity field.

In each of our Lagrangian experiments, we output the position and properties of particles at every grid-cell crossing. Since the potential temperature ($^{\circ}\text{C}$) and salinity (PSU) are defined at the center of each grid cell, TRACMASS assigns particles the average of the tracer values located at the two nearest T-points. The potential density referenced to the surface is subsequently computed using the EOS-80 non-linear equation of state (Fofonoff and Millard 1983) as in our ORCA025 configuration of NEMO (Madec 2014).

3. Northward inflow across OSNAP East

We begin by analysing the composition of the time-mean northward inflow across OSNAP East in our primary Lagrangian experiment (1976-2008). Figure 2a shows the average distribution of full-depth northward transport sampled by Lagrangian particles flowing across the OSNAP East section. Of the 64.9 Sv of total northward transport, 21.3 Sv enters via the Irminger Basin (west

252 of the Reykjanes Ridge), representing the combined transports of the Irminger Current and the
 253 Irminger Gyre. In comparison, Våge et al. (2011) used mean absolute geostrophic velocities from
 254 1991–2007 to estimate northward transports of 13 ± 3 Sv and 4.2 ± 1.9 Sv (~ 17.2 Sv in total)
 255 for the Irminger Current and the Irminger Gyre, respectively. The larger full-depth northward
 256 transport determined from Lagrangian particles is explained by the absence of compensating
 257 southward transports due to recirculation features in the interior Irminger Basin (see blue bars in
 258 Figure 2a). Figure 2b highlights a sharp density contrast between the dense northward transport
 259 of the Irminger Gyre, feeding the basin interior, and the lighter, surface-intensified transport of
 260 the Irminger Current along the western Reykjanes Ridge. These differences in density reflect the
 261 contrasting origins of the two northward currents: the southernmost limb of the Irminger Gyre
 262 advects Labrador Sea Water formed via open-ocean deep convection to the Irminger Basin interior
 263 (Lavender et al. 2000; Våge et al. 2011), whereas the Irminger Current is fed by water sourced from
 264 the NAC, which recirculates from the southward flowing East Reykjanes Ridge Current (ERRC)
 265 (Bower et al. 2002; Koman et al. 2020).

273 To the east of the Reykjanes Ridge, inflow across OSNAP East occurs via the branches of
 274 the NAC. The structure and composition of the NAC shown in Figure 2 compares favourably
 275 with observations. Each of the NAC branches is associated with a characteristic SPMW, formed
 276 during wintertime convection (McCartney and Talley 1982), whose properties reflect the relative
 277 contributions of subpolar and subtropical waters (de Boisséson et al. 2012). In the central Iceland
 278 Basin, the northern NAC branch advects 17.3 Sv of relatively cold and fresh SPMW, sourced
 279 predominantly from the Labrador Sea (de Boisséson et al. 2012). To the east, the central NAC
 280 branch, transporting 16.4 Sv, is characterised by a sharp salinity front known as the Sub-Arctic
 281 Front (SAF; Bersch et al. 1999). As the oceanographic boundary of the SPG (Bersch et al.
 282 2007), the SAF divides water of subpolar origin on the western side of the central NAC branch
 283 from subtropical-origin water to the east. The strong density-gradient across this baroclinic front
 284 produces the intensification of transport along the steep western flank of the Rockall Plateau, which
 285 resembles the quasi-permanent Hatton-Bank jet observed by Houpert et al. (2018).

286 East of the Hatton Bank, Figure 2b shows that northward flowing SPMWs become lighter as the
 287 influence of warm and saline subtropical water increases towards Scotland. The relatively weak 2.9
 288 Sv of northward transport over the Rockall Plateau likely results from the compensating transports

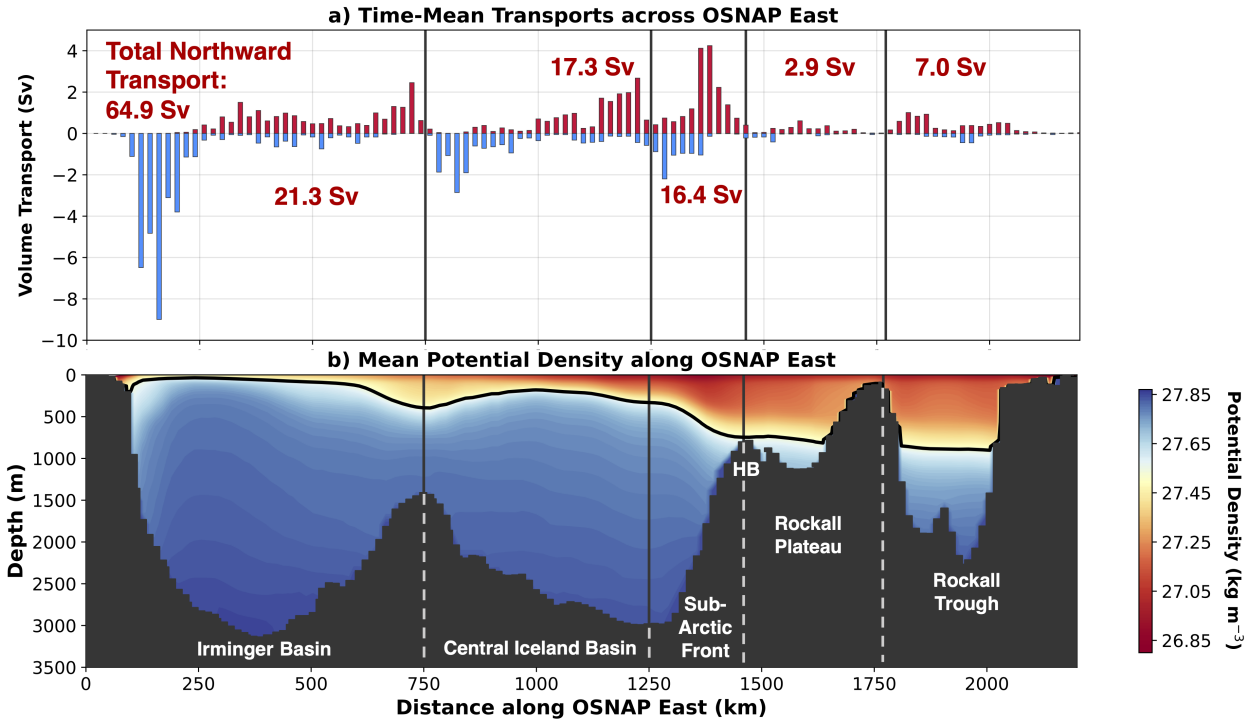


FIG. 2. Time-mean (1976-2008) volume transports and potential density at OSNAP East. a) Mean full-depth northward (red) and southward (blue) transports across OSNAP East summed using discrete bins ($\Delta x = 20$ km) along the section. Vertical dashed lines divide the inflow across the section into five geographic regions with the corresponding total northward volume transports shown. b) Mean potential density along OSNAP East overlaid by the 1976-2008 mean isopycnal of maximum Eulerian overturning (27.51 kg m^{-3}), denoting the interface between the upper and lower limbs of the AMOC. The location of the Hatton Bank is labelled along OSNAP East as HB.

of the unstable southward flow observed along the western flank of the Rockall Plateau and the northward flowing Rockall Bank jet to the east (Houpert et al. 2018). The remaining 7.0 Sv of inflow transport enters the Rockall Trough via two northward flowing boundary currents representing the southernmost branch of the NAC. This mean transport agrees closely with the recent observations of Houpert et al. (2020), who estimated that 6.6 Sv of NAC water flows northward in the Rockall Trough (2014–2018).

4. Overturning in density-space at OSNAP East

To evaluate the extent to which water masses are transformed north of OSNAP East, we first calculate the time-mean Eulerian overturning stream function in density-space in Figure 3a-c. This is constructed by averaging the monthly integrated northward and southward volume transports across the OSNAP East section in discrete potential density bins ($\Delta\sigma = 0.01 \text{ kg m}^{-3}$) between 1976-2008 (Fig. 3a). A net transport distribution in density-space (Fig. 3b) is then produced by summing the averaged inflow and outflow transport distributions in Figure 3a, before the mean overturning stream function is obtained by computing the running integral from the surface to the ocean floor following Lozier et al. (2019). The strength of the time-mean AMOC at OSNAP East, given by the maximum of the overturning stream function shown in Figure 3c, is 15.3 Sv at $\sigma_{AMOC} = 27.51 \text{ kg m}^{-3}$, which is in close agreement with the 1992-2006 average of 15.9 ± 1.9 reported by Sarafanov et al. (2012). The simulated overturning is weaker than the 2014-2018 estimate of 16.8 ± 0.6 Sv at OSNAP East (Li et al. 2021). Concomitant with the absence of NADW in the densest classes, a lighter isopycnal of maximum overturning (σ_{AMOC}) is simulated at OSNAP East compared with observations (27.55 kg m^{-3} ; Sarafanov et al. 2012; Chafik and Rossby 2019; Li et al. 2021), indicating that the upper cell of the AMOC is too shallow in the model (Danabasoglu et al. 2010). The net poleward transport across the section is 1.2 Sv, which is consistent with the estimates of 1.0-1.6 Sv of throughflow to the Arctic Ocean east of Greenland used in inverse models (Lherminier et al. 2007; Lozier et al. 2019).

To complement the traditional Eulerian overturning stream function, we next define a Lagrangian measure of the density-space overturning at OSNAP East by extending the methodology of Georgiou et al. (2020, 2021). We use the trajectories generated in our primary Lagrangian experiment to evaluate the mean water mass transformation taking place along the circulation pathways confined to the south of the Greenland-Scotland Ridge. To achieve this, we first extract the 9.8 million of the total 11.2 million numerical particles initialised across all 396 months between 1976-2008 which return to OSNAP East without crossing the Greenland-Scotland Ridge and within the maximum advection time of 7 years. For each monthly initialisation, we integrate the volume transports of these particles in discrete potential density bins ($\Delta\sigma = 0.01 \text{ kg m}^{-3}$), thereby constructing two Lagrangian transport distributions each month using the properties of particles on their northward and southward crossings of the OSNAP East section. In keeping with the Eulerian calculation

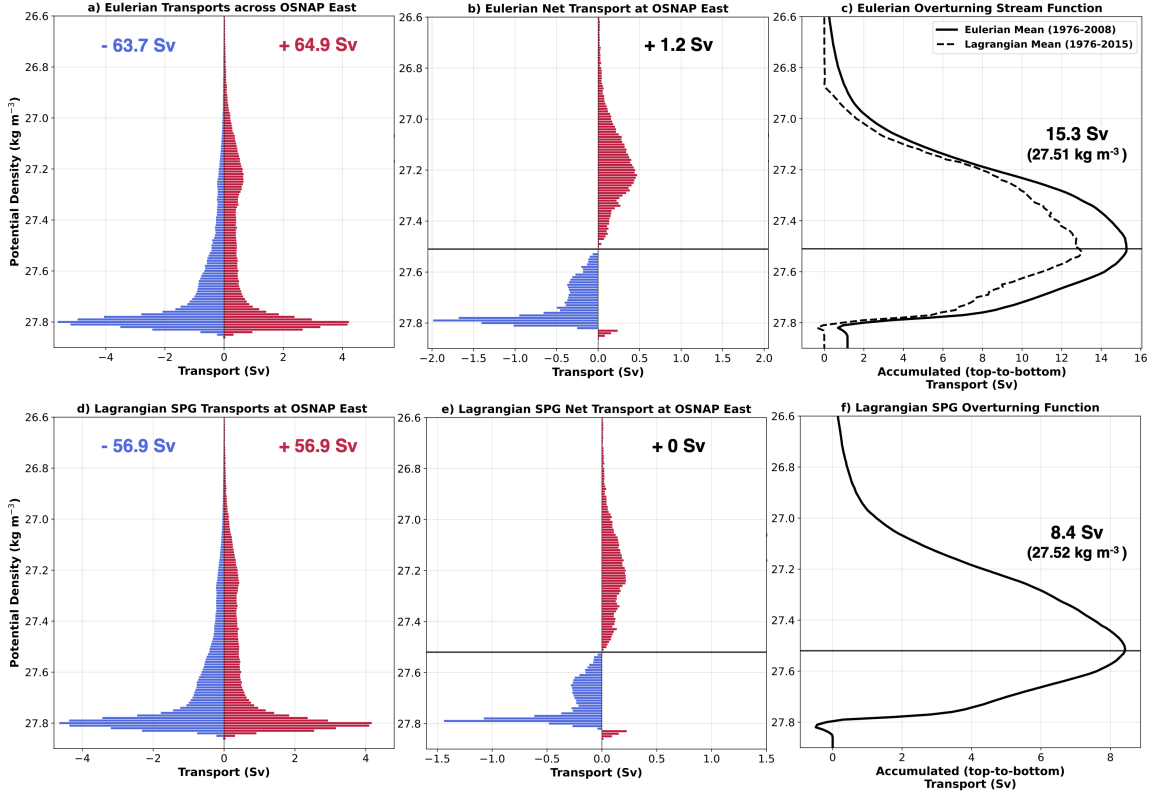


FIG. 3. Time-mean (1976 - 2008) volume transports and overturning at OSNAP East as a function of potential density (σ). a) Monthly Eulerian northward (red) and southward (blue) volume transports, integrated in 0.01 kg m^{-3} potential density bins and averaged across all 396 months. b) The net volume transport distribution across OSNAP East obtained by summing the mean northward and southward transports (a) in each potential density bin. The net throughflow to the Arctic Ocean is also shown. c) Eulerian overturning stream function (solid line) and complementary Lagrangian Overturning Function (dashed line) computed from the trajectories evaluated using 1976-2015 stationary velocity and hydrographic fields. The magnitude and isopycnal of the maximum Eulerian overturning stream function is also shown. d) Lagrangian mean northward (red) and southward (blue) volume transport distributions of the eastern SPG determined by averaging the volume transports of particles which return to OSNAP East in 0.01 kg m^{-3} potential density bins. e) Lagrangian net volume transport distribution of the eastern SPG in potential density-space. Note that no net throughflow to the Arctic Ocean is permitted. f) Lagrangian Overturning Function of the eastern SPG with the magnitude and isopycnal of maximum Lagrangian overturning shown. The horizontal (solid) lines identify the isopycnals of maximum Eulerian (b, c; $\sigma_{AMOC} = 27.51 \text{ kg m}^{-3}$) and Lagrangian (e, f; $\sigma_{SPG} = 27.52 \text{ kg m}^{-3}$) overturning.

outlined above, the time-mean northward and southward Lagrangian transport distributions (Fig. 3d) are obtained by averaging the monthly transport distributions at OSNAP East. Figure 3d shows that, on average, 56.9 Sv (87.7%) of the 64.9 Sv total northward transport across OSNAP East recirculates within the eastern SPG, south of the Greenland-Scotland Ridge. The remaining 8.0 Sv of northward transport which crosses the Greenland-Scotland Ridge is divided between the net throughflow to the Arctic Ocean (1.2 Sv) and 6.8 Sv of residual transport which would eventually return to OSNAP East either via the dense Nordic seas overflows or via the fresh East Greenland Coastal Current (EGCC). Returning to the recirculating northward transport within the eastern SPG, we next calculate a volume-conserving Lagrangian Overturning Function (LOF), $F(\sigma)$, analogously to the Eulerian overturning stream function, by taking the cumulative sum of the time-mean Lagrangian net transport distribution (Fig. 3e) from the surface to the ocean floor. The mean LOF for the eastern SPG, presented in Figure 3f, reaches a maximum overturning of 8.4 Sv at $\sigma_{SPG} = 27.52 \text{ kg m}^{-3}$, in close agreement with the value of σ_{AMOC} determined from the Eulerian overturning stream function (27.51 kg m^{-3}).

To evaluate the performance of our Lagrangian particle tracking approach, we compare our Lagrangian estimate of the overturning within the eastern SPG to steady-state volume budgets of the eastern SPNA constructed from recent observations. For consistency, we choose to express the net volume flux from the upper to the lower limb of the AMOC between OSNAP East and the Greenland-Scotland Ridge as a percentage of the net upper limb transport recorded at the OSNAP East section. The maximum Lagrangian overturning shown in Figure 3f informs us that 55% (8.4 Sv) of the time-mean net transport of the upper limb across OSNAP East (15.3 Sv shown in Fig. 3c) is transferred into the lower limb within the Iceland and Irminger Basins, south of the Greenland-Scotland Ridge. This corresponds closely with the studies of Chafik and Rossby (2019), Petit et al. (2020) and Sarafanov et al. (2012), who estimate that the Iceland and Irminger Basins are collectively responsible for 50% (9.6 Sv between 2012-2016), 52% (7.6 Sv between 2014-2016) and 60% (10.2 Sv between 2002-2008) of the overturning north OSNAP East, respectively. We therefore conclude that the Lagrangian Overturning Function accurately depicts the contribution of water mass transformation within the eastern SPG to the mean strength of the AMOC at OSNAP East.

5. Lagrangian overturning pathways in the eastern SPG

We next explore how the Lagrangian overturning is distributed across the major circulation pathways of the eastern SPG. To do this, we categorise numerical particles according to the route by which they recirculate back to the OSNAP East section. Three circulation pathways are defined geographically: particles which flow westward across the Reykjanes Ridge north of OSNAP East (*IcRo-RR-Irm*), and particles confined to the Iceland-Rockall (*IcRo-IcRo*) and Irminger Basins (*Irm-Irm*) respectively. We note that no particles with an Irminger Basin inflow return to the section east of the Reykjanes Ridge.

Figure 4 highlights the strong disparity between the distributions of northward transport and Lagrangian density-space overturning across our three circulation pathways. We find that the *IcRo-IcRo* and *Irm-Irm* pathways account for 81% (46.1 Sv) of the mean northward transport recirculating within the eastern SPG yet are collectively responsible for only 25% (2.1 Sv) of the mean Lagrangian overturning at OSNAP East. To understand the source of this disparity, we compute the net change in potential density of particles between northward and southward crossings of OSNAP East, $\Delta\sigma$, as a function of their inflow location along the section (Fig. 5). Figure 5 shows that the densification of particles decreases as the mean depth of the isopycnal of maximum Lagrangian overturning shoals with distance westward along OSNAP East. As a result, almost three-quarters (72%) of the transport recirculating within the Iceland-Rockall and Irminger Basins flows northward across OSNAP East in the lower limb of the AMOC, where, in the presence of weak diapycnal mixing (Waterhouse et al. 2014), particles overwhelmingly recirculate along isopycnals ($-0.01 \text{ kg m}^{-3} \leq \Delta\sigma \leq 0.01 \text{ kg m}^{-3}$). An important exception to this dominance of isopycnal transport, is found in the central Iceland Basin, where Figure 5 shows a concentrated region of negative diapycnal transport ($\Delta\sigma < -0.01 \text{ kg m}^{-3}$) below the isopycnal of maximum Lagrangian overturning. We attribute this to subpolar-origin particles in the lower limb of the AMOC becoming lighter on mixing with warm subtropical inflows, as previously highlighted by de Boiss  son et al. (2012). Such upwelling from the ocean interior arises from divergence along the northern branch of the NAC, whereby the obduction of subpolar water into the mixed layer replenishes SPMW advected northward (Brambilla et al. 2008).

Since the *IcRo-IcRo* and *Irm-Irm* pathways represent successive stages along one continuous SPG pathway intercepted by the OSNAP East array, we choose to consider their contributions

to the mean Lagrangian overturning collectively. In agreement with the observational studies of Thierry et al. (2008) and Petit et al. (2020), we find that *IcRo-IcRo* particles, sourced primarily from the northernmost NAC branch, undergo initial densification within the upper limb of the AMOC before flowing southward across OSNAP East in the ERRC (Fig. 4a, Fig. 5). Given that the ERRC retroflects south of 59°N (Daniault et al. 2016), this "pre-conditioned" SPMW promptly returns northward across OSNAP East via the Irminger Current. Since Figure 4c shows that inflow to the Irminger Current remains concentrated within the upper limb of the AMOC, it is hence the substantial densification experienced downstream in the Irminger Basin that is responsible for the subduction of *Irm-Irm* particles into the lower limb of the AMOC. These successive transformations of SPMW manifest in the LOFs presented in Figure 4a (blue and purple lines) through an increase in the density of maximum Lagrangian overturning from 27.26 kg m⁻³ (*IcRo-IcRo*) to 27.56 kg m⁻³ (*Irm-Irm*). In contrast, the secondary peak in Lagrangian overturning along the *IcRo-IcRo* pathway is explained by a small proportion of particles, which are transformed directly into the lower limb of the AMOC while transiting from the Rockall Trough to the ERRC.

The remaining 10.8 Sv of northward transport recirculating within the eastern SPG transits directly from the central and southern branches of the NAC to the EGC via the Reykjanes Ridge in the *IcRo-RR-Irm* pathway (Fig. 4b). Interestingly, Figure 4d shows a clear distinction between the southward outflow locations of the *IcRo-RR-Irm* and *Irm-Irm* pathways, with the latter concentrated further offshore within the EGC. Despite accounting for less than a fifth of the total SPG northward transport across OSNAP East, we find that the *IcRo-RR-Irm* pathway is responsible for three-quarters of the mean Lagrangian overturning within the eastern SPG (6.3 Sv at 27.52 kg m⁻³). This is consistent with Figure 5, which shows that, on average, particles initialised within the warm, surface-intensified core of the Sub-Arctic Front and the upper kilometre of the Rockall Trough and Plateau experience the largest density transformations during their recirculation. The *IcRo-RR-Irm* pathway also dominates the mean cross-Reykjanes Ridge transport of the SPG north of OSNAP East (12.4 Sv), which encouragingly resides between the observed estimates of Daniault et al. (2016) (11.3 ± 4.2 Sv north of 58.5°N during 2002-2012) and Petit et al. (2018) (13.6 ± 0.8 Sv between 59-62°N in 2015). Interestingly, Koman et al. (2020) reported a notably weaker cross-Reykjanes Ridge transport north of OSNAP East (~6.8 Sv) compared with previous observational studies; however, this discrepancy may partly be explained by the limitations of the Argo-altimetry

428 methodology used. The remaining 0.6 Sv of cross-Reykjanes Ridge transport is accounted for by
429 Atlantic Water particles which feed the North Icelandic Irminger Current flowing northwards over
430 the Denmark Strait (Jónsson and Valdimarsson 2005).

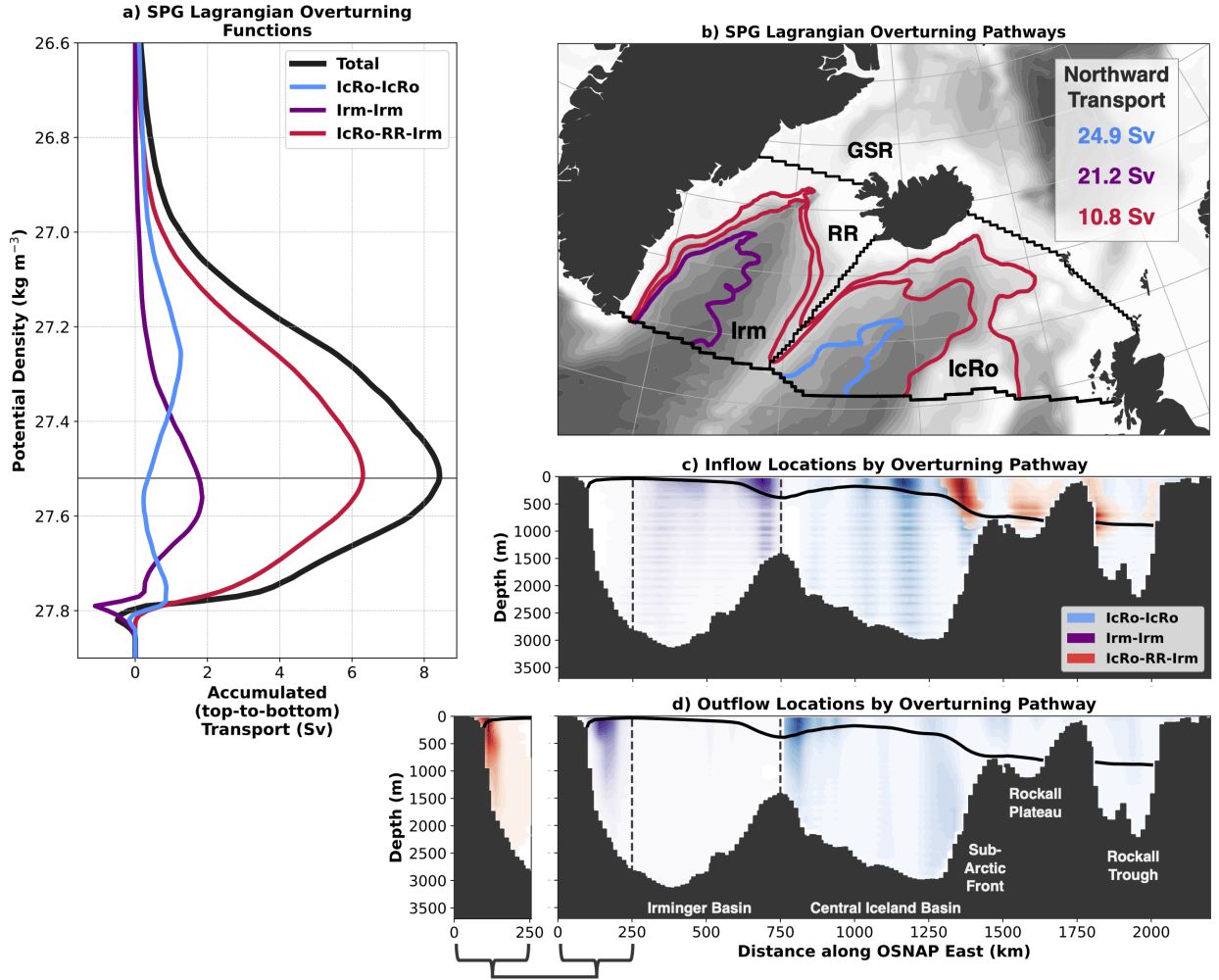


FIG. 4. Lagrangian pathways of particles recirculating back to OSNAP East within the eastern SPG. a) The total SPG Lagrangian Overturning Function decomposed by circulation pathway through the major basins: IcRo = Iceland-Rockall Basin, Irm = Irminger Basin, RR = Reykjanes Ridge. b) Example trajectories illustrating each of the three categories of circulation pathways north of the section and their respective mean northward transports across OSNAP East (Sv). Shading represents ORCA025 model bathymetry contoured every 250 m. c) Inflow and d) Outflow locations of particles along OSNAP East classified by pathway. Particle volume transports (Sv) for each pathway are averaged in discrete $x-z$ space ($\Delta z = 25$ m, $\Delta x = 25$ km) using all 396 initialisation months before normalising by the maximum mean transport recorded across all bins (darker colour shading thus indicates where, on average, transport is strongest for each overturning pathway). For clarity, the outflow locations of the *IcRo-RR-Irm* and *Irm-Irm* pathways in the EGC are presented separately in panel d. The 1976-2008 mean isopycnal of maximum Lagrangian overturning (27.52 kg m^{-3}), denoting the interface between the upper and lower limbs of the AMOC, is shown in c) and d) in bold.

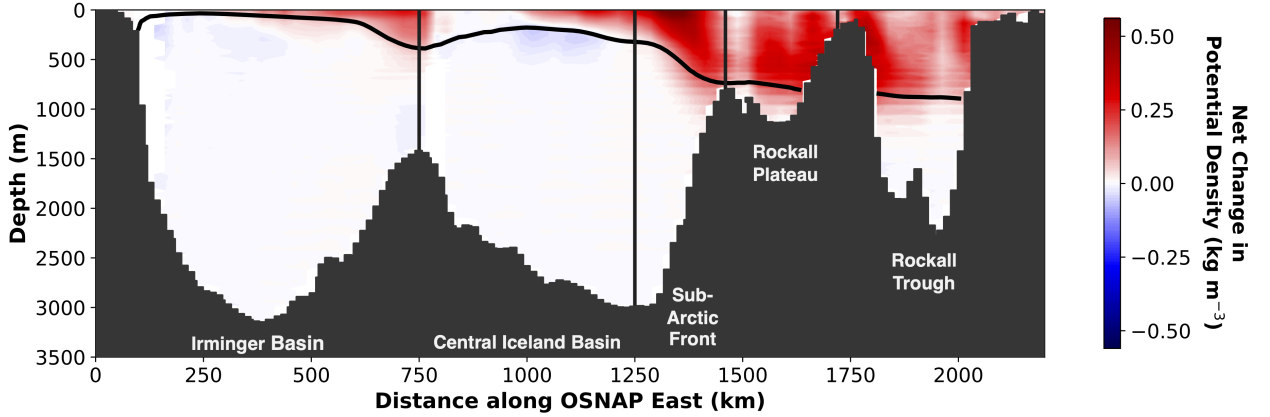


FIG. 5. Net change in potential density of particles as a function of their inflow location along OSNAP East. The net change in potential density, $\Delta\sigma$ (kg m^{-3}), between northward and southward crossings of OSNAP East is computed for recirculating particles initialised over all 396 months before averaging in discrete $x-z$ space ($\Delta z = 25$ m, $\Delta x = 25$ km). The 1976-2008 mean isopycnal of maximum Lagrangian overturning (27.52 kg m^{-3}), denoting the interface between the upper and lower limbs of the AMOC, is shown in bold. Vertical solid lines correspond to the geographical limits of the major northward currents crossing the section.

a. Pathways crossing the Reykjanes Ridge

Our finding that pathways crossing the Reykjanes Ridge directly north of 59°N are the largest contributor to the density-space overturning of the eastern SPG at OSNAP East is especially interesting given that the existence of substantial cross-ridge transport has historically been debated (e.g., Chafik et al. 2014; Petit et al. 2018). Here, we investigate the nature of these overturning pathways further and evaluate the extent to which particles are transformed east and west of the Reykjanes Ridge.

To decompose the LOF by basin, we record the potential density of each particle on crossing the ridge in order to generate two successive LOFs which capture the net density-space transformation of particles within the Iceland-Rockall and Irminger Basins before and after crossing the ridge:

$$F_{IcRo-RR-Irm}(\sigma) = F_{IcRo-RR}(\sigma) + F_{RR-Irm}(\sigma) \quad (1)$$

If $IcRo-RR-Irm$ particles reflected one pathway, continuously transformed along-stream, we would expect a decomposition in which the maxima of $F_{IcRo-RR}(\sigma)$ and $F_{RR-Irm}(\sigma)$ are equal

in magnitude yet increasing in potential density, such that the maximum of $F_{IcRo-RR-Irm}(\sigma)$ lies between them. The decomposition presented in Figure 6a is intriguing because the isopycnal of maximum Lagrangian overturning for the *IcRo-RR-Irm* pathway (27.51 kg m^{-3}) does not reside halfway between the maxima of the two constituent LOFs (*IcRo-RR*: 27.31 kg m^{-3} and *RR-Irm*: 27.52 kg m^{-3}). Instead, the maximum of the total LOF is found close to the peak of overturning within the Irminger Basin. This displacement arises from the substantial water mass transformation across isopycnals denser than those at which the maximum overturning sits in the Iceland-Rockall Basin, which contributes a substantial 2.1 Sv to the maximum Lagrangian overturning at 27.52 kg m^{-3} . This additional overturning at higher densities in the Iceland-Rockall Basin also imprints onto the distribution of *IcRo-RR-Irm* particles in T-S space presented in Figure 6b, which indicates that two distinct pathways cross the Reykjanes Ridge north of OSNAP East.

The two pathways crossing the Reykjanes Ridge can be isolated by categorising particles according to their inflow locations along OSNAP East. Of the 10.8 Sv crossing the ridge north of 59°N , we find that 8.7 Sv is sourced from the SAF and exhibits a progressive increase in potential density along stream, in close agreement with the evolution of SPMW described by Brambilla and Talley (2008). The SPMW advected along this *Ic-RR-Irm* sub-pathway is initially relatively warm ($8.7 \pm 2.0 \text{ }^\circ\text{C}$) and salty (35.2 ± 0.1), reflecting an approximately equal mixture of subtropical and subpolar waters situated either side of the SAF. Figure 7a illustrates how particles sourced from the SAF circulate cyclonically around the Iceland Basin before crossing the Reykjanes Ridge with an average potential density of $27.48 \pm 0.19 \text{ kg m}^{-3}$. This agrees closely with the density of SPMW found along the Reykjanes Ridge in both the modelling study of de Boissés et al. (2012) and the observations of Thierry et al. (2008) between 1990-2006. SAF particles undergo further densification along the northern boundary of the Irminger Basin, including subduction into the lower limb of the AMOC on the edge of the EGC. The resulting entrainment into the EGC, coupled with the pathway's intermediate density ($27.62 \pm 0.20 \text{ kg m}^{-3}$) on returning to OSNAP East, suggests that SPMWs originating from the SAF are the likely source of upper Irminger Sea Intermediate Water, recently identified by Le Bras et al. (2020).

The gradual densification exhibited along the SAF pathway is largely explained by the small median depth change of SPMW particles ($\Delta z \approx +55 \text{ m}$), which, in the presence of sloping isopycnals, enables water masses to undergo continuous cooling and freshening during recirculation. Although

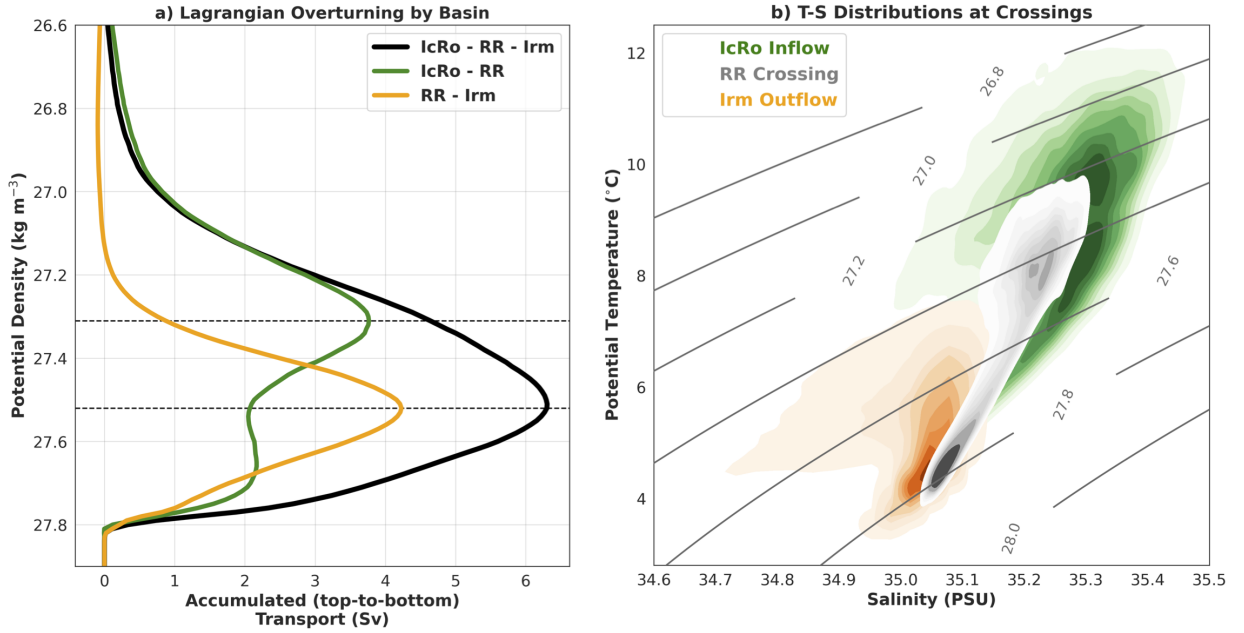


FIG. 6. Water mass transformation along the pathways crossing the Reykjanes Ridge directly north of OSNAP East. a) The Lagrangian Overturning Function of the *IcRo-RR-Irm* pathway (black line) decomposed by basin; overturning in the Iceland-Rockall basin (*IcRo-RR*) is shown in green and the Irminger basin (*RR-Irm*) in orange. Note that taking the sum of the two basin LOFs (green and orange lines) recovers the *IcRo-RR-Irm* pathway LOF (black). b) Density distribution of particle potential temperature and salinity at inflow (*IcRo*, green), on crossing the Reykjanes Ridge (*RR*, grey) and at outflow (*Irm*, orange) for the *IcRo-RR-Irm* pathway. Contours, corresponding to iso-proportions of the density, are plotted with an interval of 0.1, such that 10% of all numerical particles are contained within the shaded region between any two contours. Overlaid potential density contours are computed using EOS80 as in the NEMO model.

this implies that density compensation occurs within the subpolar gyre (Xu et al. 2016; Zou et al. 2020b), we find that thermal changes dominate the diapycnal transformation, in agreement with estimates of the surface-forced overturning due to air-sea buoyancy fluxes (e.g., Marsh 2000; Desbruyères et al. 2019). The largely horizontal *Ic-RR-Irm* sub-pathway accounts for 4.8 Sv of the maximum Lagrangian overturning at OSNAP East, and thus corresponds closely with the horizontal component of overturning estimated by Zhang and Thomas (2021) using OSNAP observations (5.6 Sv).

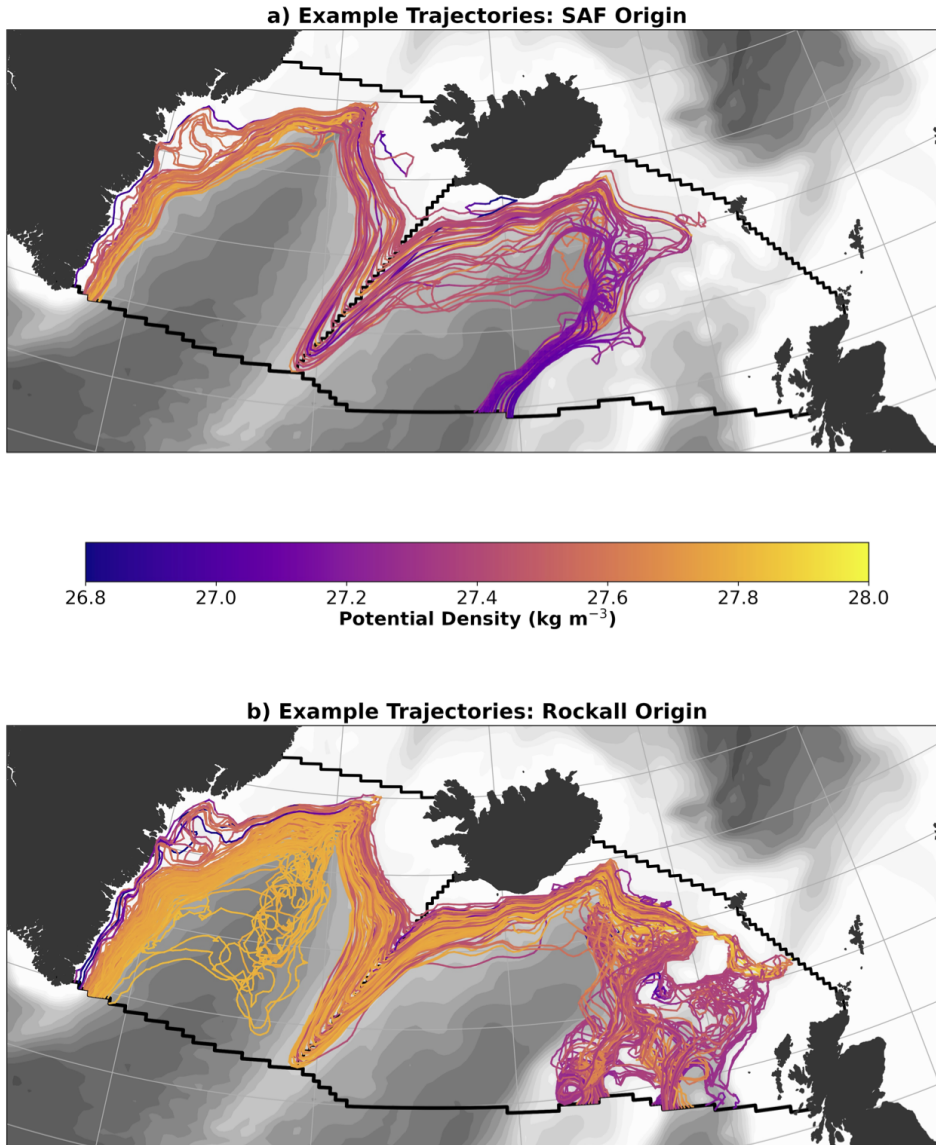


FIG. 7. Example trajectories for the two principal circulation pathways crossing the Reykjanes Ridge north of OSNAP East. The potential density evolution along 50 randomly sampled trajectories originating from a) the Sub-Arctic Front and b) the Rockall Trough and Plateau is shown in colour. Trajectories are superimposed on the ORCA025 model bathymetry contoured every 250 m.

The remaining 2.1 Sv of the *IcRo-RR-Irm* pathway flows northward across OSNAP East at intermediate depths via the inflows to the Rockall Trough and over the Rockall Plateau. Although the water masses transported along this *Ro-RR-Irm* sub-pathway are overwhelmingly of subtropical

origin, they are found to be denser on arrival to the section compared with that of *Ic-RR-Irm* particles owing to their greater salinity (35.3 ± 0.1). Figure 7b shows that particles are advected northwards feeding the 500-1000 m "entrainment zone" in the northern Iceland Basin (Dickson et al. 2002; Sarafanov 2009) before undergoing dramatic cooling and freshening near the Faroe Bank Channel. This step-change in water properties along the Rockall pathway (Fig. 6b) closely resembles the formation of Icelandic Slope Water (ISW) (Van Aken and De Boer 1995; Read 2000; Holliday et al. 2009): ISW is a water mass formed when ISOW descending the Iceland-Faroes Ridge entrains ambient SPMW. This interpretation of the *Ro-RR-Irm* sub-pathway is additionally supported by the recent observations of Petit et al. (2018), who showed that ISW was the second largest contributor to the westward flow across the Reykjanes Ridge between 50°N and 63°N . After following the 1000 m bathymetric contour around the northern Iceland Basin (Fig. 7b), particles reach the Reykjanes Ridge with an average density of $27.70 \pm 0.12 \text{ kg m}^{-3}$, consistent with their large median depth change of +380 m. In contrast to the SAF pathway, particles experience minimal further densification in the Irminger Basin before returning to OSNAP East via the EGC. As a result of their greater depth, particles additionally show a greater propensity to follow deep interior pathways tracing the western flank of the Reykjanes Ridge before being re-entrained into the boundary current (Fig. 7b).

b. Timescales of Lagrangian overturning in the eastern SPG

One of the most valuable properties of the density-space LOF, as applied here, is that it integrates across particles with recirculation times ranging from days to years. We can therefore examine the temporal structure underlying the time-mean LOF of the eastern SPG and diagnose the dominant advective timescales over which water mass transformation takes place north of OSNAP East. Throughout our subsequent discussion, we choose to define the times taken to recover 50% ($\tau_{50\%}$) and 90% ($\tau_{90\%}$) of the maximum Lagrangian overturning as measures of the characteristic overturning timescale for each of our circulation pathways.

In Figure 8a we present the Lagrangian overturning of the eastern SPG as a function of the time particles spend north of OSNAP East, such that at any given time only the subset of all recirculating particles which have already returned to the section are included in the calculation. Since only particles which recirculate south of the Greenland-Scotland Ridge are included in this calculation,

543 we reserve discussion of the overturning timescales associated with Nordic seas overflows for
544 Section 6b. Remarkably, we find that three-quarters of the maximum Lagrangian overturning
545 within the eastern SPG (at 27.52 kg m^{-3}) can be explained by particles which spend 1.4 years
546 or less north of OSNAP East. A further 5.6 years is required to recover the remaining 25% of
547 the maximum Lagrangian overturning, along with the majority of SPG overturning in the highest
548 density classes ($> 27.7 \text{ kg m}^{-3}$).

549 Previous Lagrangian studies have considered the circulation and overturning timescales as equiv-
550 alent (e.g. Georgiou et al. 2020, 2021). However, Figure 8b shows that, on average, 50% of the
551 northward transport returns to OSNAP East in just 0.6 years, approximately half of the time taken
552 to recover the equivalent proportion of the maximum Lagrangian overturning ($\tau_{50\%} = 1.0 \text{ yrs}$). This
553 large disparity between the overturning and circulation timescales indicates that isopycnal trans-
554 port, predominantly circulating in the lower limb of the AMOC (Fig. 5), must, on average, return
555 to OSNAP East more quickly than water which is transformed across isopycnals. The *Irm-Irm*
556 pathway is an important exception, however, given that isopycnal transport in the Irminger Gyre
557 recirculates to OSNAP East more slowly than the adjacent Irminger Current, despite its shorter
558 path length (not shown).

559 Figure 8b also shows that the relationship between the maximum Lagrangian overturning and
560 recirculating volume transport is not consistent over the duration of our primary Lagrangian
561 experiment. Instead, the evolution of SPG overturning at OSNAP East is characterised by episodes
562 of strong diapycnal transport associated with the return of each of the major overturning pathways
563 identified in Section 5a. The rapid accumulation of Lagrangian overturning between 0.5 - 1.5 years
564 following northward flow across OSNAP East is dominated by *Irm-Irm* and *Ic-RR-Irm* pathways
565 of the eastern SPG. The initial pulse of overturning recovered at OSNAP East is explained by
566 particles recirculating along the *Irm-Irm* pathway, which are advected through the Irminger Basin
567 on seasonal timescales ($\tau_{50\%} = 0.5 \text{ yrs}$). Meanwhile, water mass transformation along the *Ic-RR-Irm*
568 pathway is divided evenly between particles recirculating on sub-annual and interannual timescales
569 ($\tau_{50\%} = 1.0 \text{ yrs}$). As the largest contributor within the eastern SPG to the mean strength of the
570 AMOC at OSNAP East, the especially narrow distribution of overturning times exhibited by *Ic-*
571 *RR-Irm* particles ($\tau_{90\%} = 1.6 \text{ yrs}$) supports the conclusion of Petit et al. (2020) that surface buoyancy
572 loss over the Irminger and Iceland Basins drives diapycnal fluxes with minimal lag.

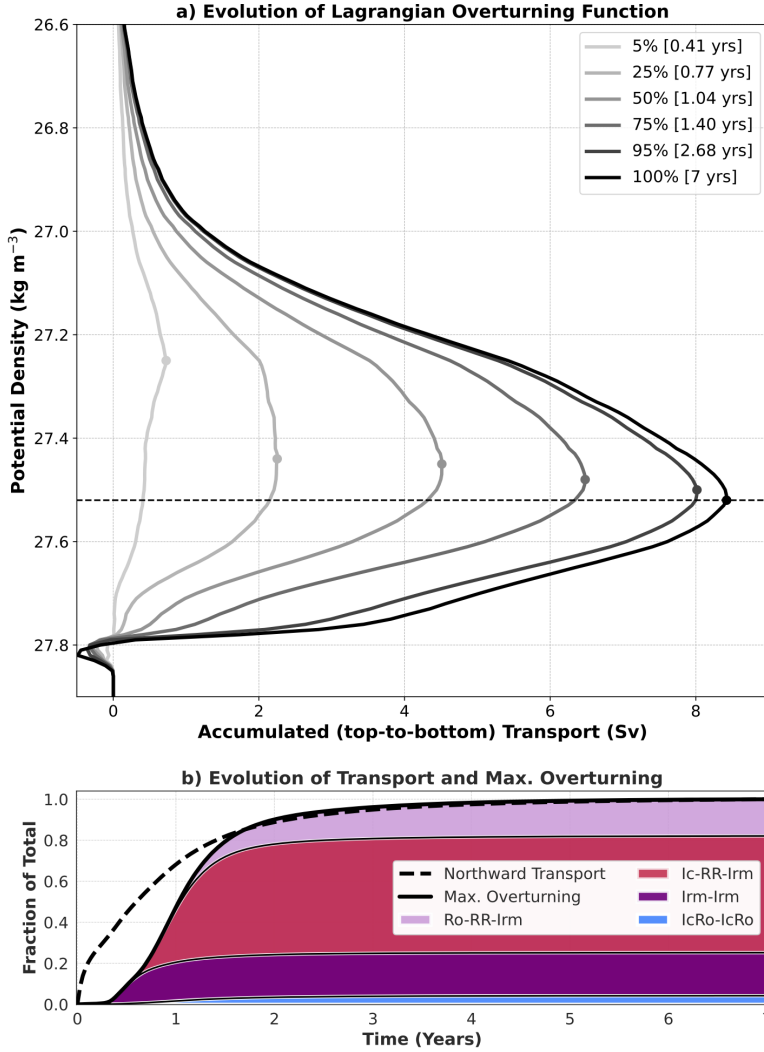


FIG. 8. Evolution in time of Lagrangian overturning of the eastern SPG at OSNAP East. a) Lagrangian Overturning Function evaluated as a function of time elapsed following northward flow across OSNAP East, with the maximum denoted for each profile (dots). The horizontal dashed line in (a) corresponds to the isopycnal of maximum Lagrangian overturning (27.52 kg m^{-3}) once 7 years have elapsed. b) Normalised cumulative volume transport (black-dashed) and Lagrangian overturning (black-solid) at the 27.52 kg m^{-3} isopycnal as a function of time elapsed following northward flow across OSNAP East. The proportion of the maximum Lagrangian overturning accounted for by each of the eastern SPG circulation pathways is shaded.

Once 1.5 years have elapsed following northward flow across OSNAP East, a more gradual accumulation of Lagrangian overturning is evident in Figure 8b, attributable to the deep *IcRo-IcRo* ($\tau_{90\%} = 2.6 \text{ yrs}$) and *Ro-RR-Irm* ($\tau_{90\%} = 3.4 \text{ yrs}$) pathways. The longer overturning timescale of both

583 pathways is associated with the entrainment of SPMW, sourced from the Rockall Trough, into the
 584 Norwegian Seas overflow, which subsequently returns to OSNAP East at depth either via the ERRC
 585 (*IcRo-IcRo*) or the EGC (*Ro-RR-Irm*) (see Fig. 4d). Our finding that entrainment can contribute
 586 to deep water formation in the northern Iceland Basin on subdecadal timescales agrees with the
 587 recent observational study of Devana et al. (2021). Those authors estimated a total advection time
 588 of 1.5 - 2.5 years for upper ocean anomalies in the Iceland Basin to be entrained into the overflows
 589 and return to OSNAP East in the ISOW layer. Although the timescale estimated by Devana et al.
 590 (2021) agrees closely with those determined from Lagrangian particles above, we note that a formal
 591 comparison is impeded by the model's inability to form ISOW in the observed density range due
 592 to excessive entrainment south of the Greenland-Scotland Ridge (MacGilchrist et al. 2020).

593 **6. Lagrangian overturning in stationary fields**

594 *a. Comparing the mean Lagrangian overturning in the eastern SPG using time-evolving and* 595 *stationary fields.*

596 An important limitation of our primary Lagrangian experiment is our inability to explicitly
 597 resolve the overturning pathways of the Nordic seas overflows within the relatively short 7-year
 598 advection time. To diagnose the contribution of the Nordic seas overflow pathways to the mean
 599 strength of the AMOC at OSNAP East, we therefore choose to replicate our primary Lagrangian
 600 experiment using time-averaged velocity and tracer fields (1976-2015). There are two principal
 601 advantages of using a stationary velocity field in our Lagrangian analysis. Firstly, trajectory
 602 computations and analysis are more efficient since using a single time-averaged velocity field
 603 eliminates the need for multiple particle initialisations. Secondly, since stationary velocity and
 604 tracer fields are, by definition, time-independent, their use permits an arbitrary maximum particle
 605 advection time. Here, we choose to advect particles for a maximum of 60-years, thereby exceeding
 606 the length of the historical period simulated by our ocean model hindcast by a further two decades.
 607 Importantly, Drijfhout et al. (2003) showed that neglecting eddy-induced transports through the use
 608 of a time-averaged Eulerian velocity field resulted in severe biases in the Lagrangian overturning
 609 pathways and transports in the South Atlantic. It is therefore necessary to test our stationary fields
 610 approach by comparing the structure of the time-mean Lagrangian overturning in the eastern SPG
 611 determined from both time-evolving and time-averaged fields.

620 To ensure consistency in our comparison of the two Lagrangian experiments, the diagnostics
621 presented in Figure 9 include only the particles which return to OSNAP East within the eastern SPG
622 and within 7 years of flowing northwards across the section. Figure 9a shows that, while the absence
623 of time-varying transports results in a small 0.5 Sv overestimation of the maximum Lagrangian
624 overturning at 27.52 kg m^{-3} , the mean LOFs generated from stationary and time-evolving fields
625 are in remarkably close agreement.

626 On partitioning the maximum Lagrangian overturning in the eastern SPG between the four
627 circulation pathways defined in Section 5, we encouragingly find that the composition of SPG
628 overturning at OSNAP East is reproduced using stationary fields, including the dominance of the
629 pathways crossing the Reykjanes Ridge. The median recirculation time and northward transport
630 advected along our dominant *Ic-RR-Irm* pathway are especially well represented in stationary fields
631 (Fig. 9c-d), suggesting that eddy-induced transports make only a limited contribution to the mean
632 overturning along this route. In contrast, the northward transport advected along the *IcRo-IcRo*
633 and *Irm-Irm* pathways are found to be underestimated by 10.2 Sv and 5.2 Sv, respectively, in
634 our stationary fields experiment. We attribute this considerable underestimation to our averaging
635 over the seasonal cycle, given that observational studies find substantial transport variations in
636 both the Irminger and Iceland-Rockall Basins on seasonal timescales (Gary et al. 2011; de Jong
637 et al. 2020). As a further consequence of our smoothing of seasonal variations in the velocity
638 field of the eastern SPG, Figure 9d shows a notable increase in the median recirculation times of
639 the *IcRo-IcRo* and *Irm-Irm* pathways when using stationary fields. Interestingly, the maximum
640 overturning contribution of the *Irm-Irm* pathway remains in broad agreement between our two
641 Lagrangian experiments (Fig. 9b), suggesting that seasonally transformed particles recirculating
642 within the Irminger Basin do not contribute substantially to the mean strength of the AMOC at
643 OSNAP East. In the Iceland-Rockall Basin, the obscuring of wintertime transformation into the
644 lower limb of the AMOC in time-averaged fields yields a negative overturning contribution for the
645 *IcRo-IcRo* pathway, corresponding to the steady obduction of water into the upper limb along the
646 northern NAC branch (see Fig. 5).

647 In spite of the biases discussed above, we conclude that the structure of the time-mean overturning
648 at OSNAP East is sufficiently well represented in stationary velocity and tracer fields to justify
649 their use in investigating the pathways of the Nordic seas overflows.

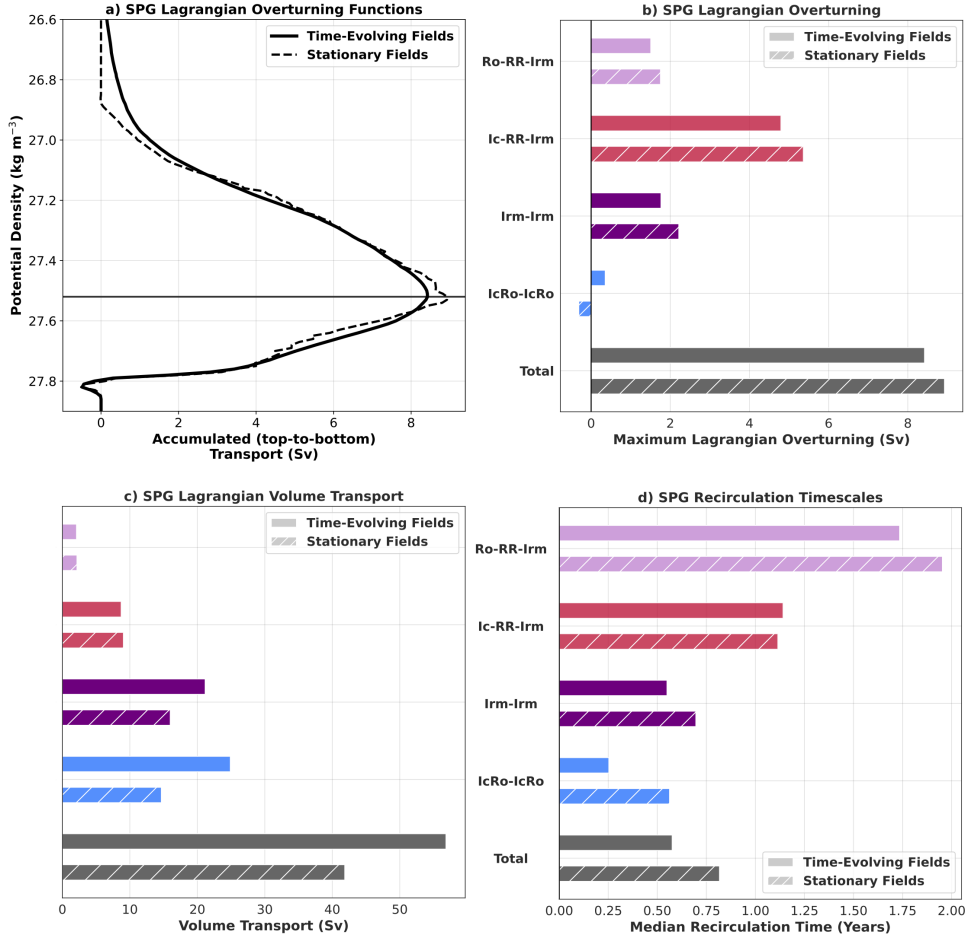


FIG. 9. Lagrangian overturning diagnostics in the eastern SPG determined from time-evolving and stationary fields experiments. a) Time-mean Lagrangian Overturning Functions for the eastern SPG calculated from ensembles of trajectories advected by time-evolving (solid line) and stationary (dashed line) velocity and tracer fields. The solid line at 27.52 kg m^{-3} identifies the shared isopycnal of maximum Lagrangian overturning in the eastern SPG. (b-d) The Lagrangian overturning at 27.52 kg m^{-3} , total northward transport across OSNAP East, and median recirculation time are decomposed into the four circulation pathways of the eastern SPG as defined in Section 5. Diagnostics determined from stationary velocity and tracer fields are distinguished using hatched bars.

b. Pathways crossing the Greenland-Scotland Ridge.

We explore the nature of overturning along the pathways of the Nordic seas overflows by considering all of the trajectories which return to OSNAP East within the maximum 60 year advection time of our second (time-invariant) Lagrangian experiment. Over the entire duration of

the experiment, 94.2% of the total northward transport initialised along OSNAP East returns to the section, allowing us to recover 13.0 Sv of the mean Lagrangian overturning in density-space (Fig. 10a). It should be noted that, since the mean LOF, by definition, cannot include the 1.2 Sv net throughflow to the Arctic we would not expect the maximum Lagrangian overturning to converge towards the maximum of the Eulerian stream function shown in Figure 3c (15.3 Sv), irrespective of our choice of the maximum advection time.

The Nordic seas overflows are captured within the 4.3 Sv sourced from the SAF and Rockall Trough, which flows northward across the Greenland-Scotland Ridge before returning to OSNAP East either via the Iceland Basin or the Irminger Sea (hereafter the *IcRo-GSR-Ic/Irm* pathway). Although the transport advected along this pathway is considerably less than the observed 8.0 ± 0.7 Sv Atlantic inflow transport crossing the Greenland-Scotland Ridge northwards (Østerhus et al. 2019), we note that this does not include the additional 2.9 Sv carried by particles which do not return to OSNAP East within 60 years. This remaining transport is composed of 1.2 Sv net throughflow to the Arctic Ocean (see Section 4) and 1.7 Sv of residual transport, which would be expected to return to OSNAP East given a sufficiently long particle advection time. On combining this outstanding transport with the transport of the *IcRo-GSR-Ic/Irm* pathway, we obtain revised estimate of the total cross Greenland-Scotland Ridge transport of 7.2 Sv, in closer agreement with observations. Figure 10a shows that, within the 60-year advection time of our secondary Lagrangian experiment, particles transformed within the Nordic seas collectively contribute 3.9 Sv to watermass transformation into the lower limb of the AMOC. The remaining 0.4 Sv of the total 4.3 Sv of recirculating transport flowing across the Greenland-Scotland Ridge is found to return southward across OSNAP East in the upper limb of the AMOC via the fresh EGCC.

Figure 10b presents the T-S distributions of overflow particles on their northward and southward crossings of both OSNAP East and the Greenland-Scotland Ridge. Concurrent with our earlier findings, the Iceland-Rockall Basin is shown to play a critical role in cooling and freshening subtropical waters en route to the Nordic seas. On crossing the Greenland-Scotland Ridge, particles represent SPMW of intermediate density ($27.37 \pm 0.14 \text{ kg m}^{-3}$), which is distinctly lighter than that crossing the Reykjanes Ridge as observed by Brambilla and Talley (2008). Watermass transformation in the Nordic seas is dominated by intense surface heat loss which is concentrated within the Norwegian Current and along the boundaries of the Greenland and Iceland Seas. On

684 returning to the Greenland-Scotland Ridge, *IcRo-GSR-Ic/Irm* particles have, on average, been
 685 cooled to 2.2 ± 1.5 °C, yielding a potential density (27.83 ± 0.19 kg m⁻³) within the observed
 686 range for overflow waters (Dickson and Brown 1994). South of the ridge, the poor representation
 687 of both advective and sub-grid scale overflow processes, which are well-established biases of
 688 numerical models (Wang et al. 2015), result in excessive entrainment of ambient Atlantic waters
 689 by the overflows. The associated warming and salinification (Fig. 10b) reduces the average
 690 potential density of overflow particles to 27.70 ± 0.16 kg m⁻³ and thus directly imprints onto
 691 the structure of the density-space overturning downstream, where the southward transport in the
 692 observed density range of the overflows is ~ 11 Sv less than found in observations (Sarafanov et al.
 693 2012). Furthermore, the unrealistically large diapycnal mixing between the overflows and ambient
 694 Atlantic water explains the absence of deep stratification (MacGilchrist et al. 2020) and hence the
 695 shallower upper cell of the AMOC in this model (see also Roberts et al. 1996; Winton et al. 1998).

696 We next distinguish between distinguish between the water mass varieties that are equivalent to
 697 DSOW and ISOW in the model (albeit found at lighter densities) by defining the former (latter)
 698 as *IcRo-GSR-Ic/Irm* particles which return to OSNAP East in the lower limb of the AMOC via
 699 the sills west (east) of Iceland. It should be noted that this definition excludes particles flowing
 700 southwards in the EGCC. Figure 10c shows that ISOW particles (1.3 Sv) predominantly originate
 701 from the surface inflows to the Rockall Trough, whereas DSOW (2.6 Sv) particles are sourced
 702 approximately equally from the warm, subtropical inflows to the SAF and below 250 m over the
 703 Rockall Plateau. Since, by definition, all of the transport advected along our two overflow pathways
 704 is transformed from the upper to the lower limb of the AMOC north of OSNAP East, it follows
 705 that DSOW contributes twice as much as ISOW to the mean Lagrangian overturning at 27.52 kg
 706 m⁻³ over the duration of our stationary fields experiment (see corresponding LOFs in Figure 10a).
 707 Importantly, it remains unclear how the residual 1.7 Sv of non-recirculating transport, which does
 708 not return to OSNAP East on entering the Nordic seas, is distributed between DSOW, ISOW and
 709 the EGCC. On returning to OSNAP East, DSOW is transported southwards below the fresh waters
 710 of the East Greenland shelf in the EGC and to a lesser extent through deep interior pathways on
 711 the western flank of the Reykjanes Ridge. Meanwhile, the export of ISOW across OSNAP East is
 712 divided almost equally between the ERRC in the western Iceland Basin and at depth in the EGC,
 713 offshore of DSOW. This distribution contrasts with recent observations, which found no substantial

cross-Reykjanes Ridge transport of ISOW north of the Bight Fracture Zone (Petit et al. 2018), and hence north of OSNAP East. One likely explanation for this discrepancy, proposed in the modelling study of Xu et al. (2010), is that the simulated ISOW is too light compared with observations, and thus flows over shallower fractures in the Reykjanes Ridge north of 59°N. In reality, approximately half of the 5.3 ± 0.4 Sv of ISOW flowing southward across OSNAP East in the ERRC (2014-18) is derived from the entrainment of SPMW and Labrador Sea Water in the northern Iceland Basin (Johns et al. 2021). However, we find negligible along-stream transformation of *IcRo-IcRo* particles within or above the observed ISOW density range (Fig. 4a), suggesting that excessively entrained SPMWs are advected unrealistically by pathways crossing the Reykjanes Ridge (*Ro-RR-Irm*) within the model.

A further distinction between ISOW and DSOW varieties can be made by examining the dominant advective timescales on which overflow particles are overturned north of OSNAP East. Figure 10d shows that, while 90% of the Lagrangian overturning along the ISOW pathway can be explained by particles which spend 37.2 years or less north of OSNAP East, almost an additional decade ($\tau_{90\%} = 45.8$ yrs) is required to accumulate the equivalent proportion of the overturning along the DSOW pathway. This difference in overturning timescales is explained by the fact that DSOW particles are twice as likely (82%) to enter the Arctic Ocean during their recirculation compared with ISOW particles (41%), and thus spend a greater amount of time north of the Greenland-Scotland Ridge (44.8 years for DSOW compared with 34.9 years for ISOW). We also find that 92% of the residual overflow transport (1.7 Sv), requiring more than 60 years to return to OSNAP East, enters the Arctic Ocean through either the Fram Strait or the Barents Sea. Our inability to recover these residual overflow particles within the duration of our Lagrangian experiment is hence unsurprising, given that recent chemical tracer studies estimate that Atlantic Waters can spend between 30-50 years circulating within the Arctic Ocean before returning to the Fram Strait (Stöven et al. 2016; Wefing et al. 2021).

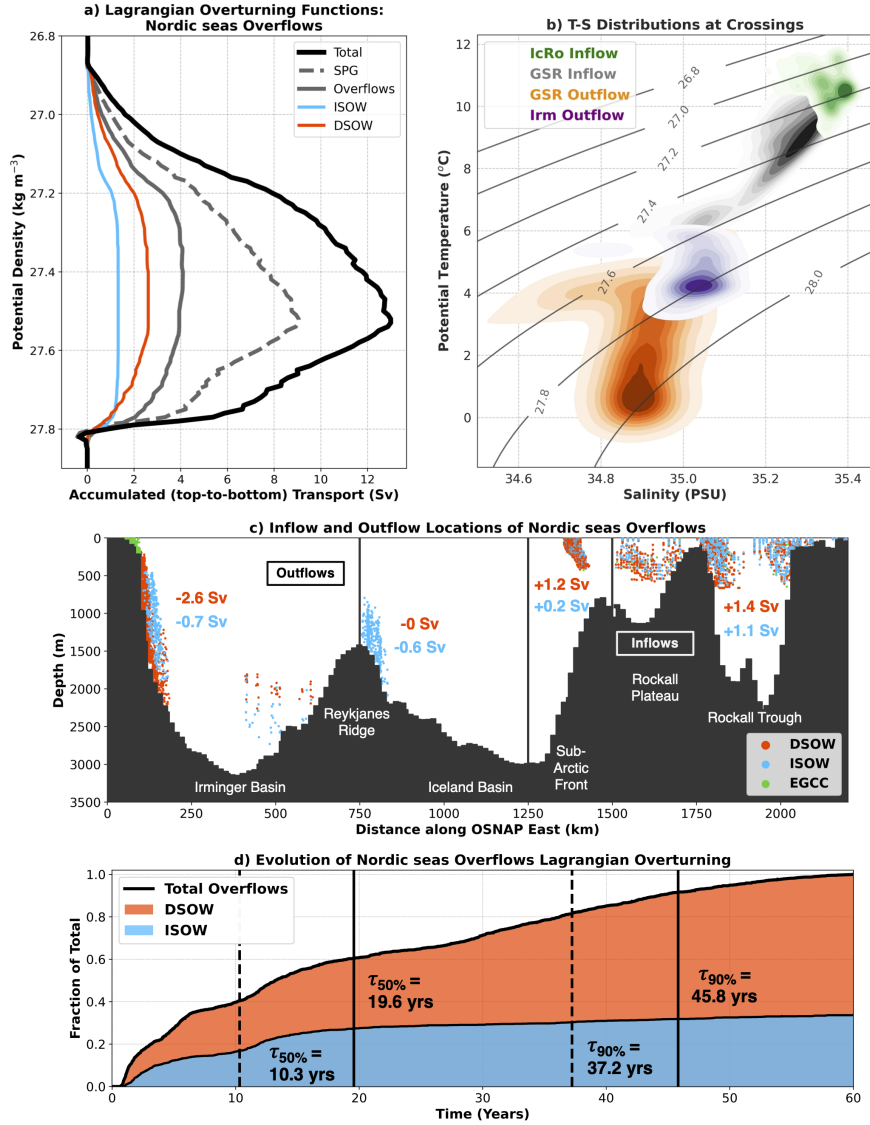


FIG. 10. Lagrangian overturning, transports and timescales for particles flowing northward across the Greenland-Scotland Ridge. a) The total LOF at OSNAP East determined using stationary fields decomposed into the contributions made by the eastern SPG and the Nordic seas overflows. The Lagrangian overturning of the Nordic seas overflows is further divided between DSOW and ISOW varieties. b) Density distribution of particle potential temperature and salinity at inflow, on northward and southward crossings of the Greenland-Scotland Ridge, and on return to OSNAP East for the *IcRo-GSR-Ic/Irm* pathway. Contours, corresponding to iso-proportions of the density, are plotted with an interval of 0.1, such that 10% of all particles are contained within the shaded region between any two contours. c) Inflow and Outflow locations of DSOW and ISOW particles along OSNAP East. The particles which return to OSNAP East via the fresh EGCC are shown in green. d) Normalised cumulative Lagrangian overturning of the Nordic seas overflows at the 27.52 kg m^{-3} isopycnal as a function of time elapsed following northward flow across OSNAP East.

7. Discussion and conclusions

In this study, we demonstrate how Lagrangian particle tracking can be employed to partition the density-space overturning across a trans-basin section amongst the circulation pathways of the subpolar AMOC. In this first application of our Lagrangian approach, we explore the structure of the time-mean overturning circulation in the eastern SPNA using a global, eddy-permitting ocean hindcast simulation (ORCA025-GJM189). By advecting particles from the northward inflows across OSNAP East using both time-evolving and stationary velocity and tracer fields, coupled with a simple parameterisation of vertical convective mixing, we quantify how water mass transformation along the circulation pathways of the eastern SPG and Nordic seas overflows projects onto overturning at OSNAP East. We show how the Lagrangian Overturning Function, complementing the traditional Eulerian stream function, can be used to diagnose the extent to which particles are transformed in each basin and identify the dominant advective timescales of the overturning circulation in the eastern SPNA.

In our primary Lagrangian experiment using time-evolving fields, we evaluate the trajectories of more than 11.2 million numerical particles initialised over 396 months between 1976-2008 to investigate the overturning pathways of the eastern SPG. Our analysis shows that 55% (8.4 Sv) of the time-mean overturning recorded at OSNAP East takes place south of the Greenland-Scotland Ridge, underscoring the dominant role of the SPG in water mass transformation (Desbruyères et al. 2019; Menary et al. 2020; Petit et al. 2020). Through a decomposition of the Lagrangian Overturning Function, we show that the SPG pathways crossing the Reykjanes Ridge north of OSNAP East make the largest contribution to mean strength of the AMOC at the section. The principal overturning pathway, accounting for 4.8 Sv of the maximum overturning, is sourced from the central NAC branch along the SAF, and undergoes continuous densification by circulating horizontally across sloping isopycnals. Moreover, since particles are subducted into the lower limb of the AMOC on the edge of the EGC and overturn rapidly in less than 2 years, we suggest that the SAF is the likely source of upper Irminger Sea Intermediate Water recently observed by Le Bras et al. (2020).

The short overturning timescales of the eastern SPG pathways are dynamically important since they govern the rate at which density anomalies can propagate through the Iceland and Irminger Basins, and thus imprint onto the overturning measured at OSNAP East. The SPNA exhibits large-

780 scale thermohaline variability on decadal timescales (Holliday 2003; Hátún et al. 2005; Lozier
781 et al. 2008; Desbruyères et al. 2021), forced in part by abrupt transitions in the North Atlantic
782 Oscillation (NAO, Hurrell 1995). Following the sharp transition to a strong positive phase of the
783 NAO in 2012, the persistence of negative wind stress curl increased the export of freshwater from
784 the Labrador and Newfoundland shelves into the branches of the NAC (Holliday et al. 2020). The
785 cold and fresh upper ocean anomalies, aided by the eastward migration of the SAF in response to
786 strengthened cyclonic wind stress curl, arrived in the Iceland Basin and Rockall Trough in 2015
787 (Holliday et al. 2020). Simultaneously, cold and dense anomalies formed by enhanced wintertime
788 heat loss over the central Labrador Sea in 2014-15 (Yashayaev and Loder 2016) arrived in the
789 upper Irminger Sea, yielding a marked strengthening of the AMOC at OSNAP East in the ensuing
790 spring (Chafik et al. 2022; Roussenov et al. 2022). However, this positive overturning anomaly was
791 relatively short-lived owing to the rapid propagation of the aforementioned cold and fresh upper
792 ocean anomalies along the boundary current of the eastern SPG. According the recent observational
793 study of Biló et al. (2022), fresh anomalies advected in the NAC reached the Reykjanes Ridge in
794 early 2016 before transiting to the EGC mooring positioned along OSNAP East in a further 6-11
795 months. This implies a total advection time of between 1.5-1.9 years for the freshening signal
796 to propagate from the Iceland Basin to the Irminger Sea, in close agreement with our dominant
797 overturning timescale of 1.6 years along the *Ic-RR-Irm* pathway.

798 Density anomalies have also been shown to propagate from the upper to the deep ocean via the
799 entrainment of SPMW by the Iceland-Scotland overflows (Dickson et al. 2002; Sarafanov 2009;
800 Devana et al. 2021). In particular, Sarafanov et al. (2010) attributed the persistent salinification of
801 ISOW during the late 1990s to the NAO-induced increase in subtropical input to the eastern SPNA.
802 Here, we have identified a deep overturning pathway along which upper intermediate waters of
803 subtropical origin undergo dramatic cooling and freshening south of the Iceland-Scotland Ridge.
804 The resulting water mass, resembling dense ISW (Van Aken and De Boer 1995; Read 2000),
805 crosses the Reykjanes Ridge north of 59°N before returning to OSNAP East via the EGC and deep
806 interior pathways. Our conclusion that it takes 3.4 years for 90% of the overturning to occur along
807 this pathway aligns with the recent finding of Devana et al. (2021), who showed that NAO-induced
808 freshening of the upper ocean can propagate into the deep overflows via turbulent entrainment on
809 subdecadal timescales.

810 To overcome our inability to recover the recirculating transport associated with the Nordic seas
 811 overflows in our primary Lagrangian experiment, we conduct a supplementary experiment using
 812 time-averaged velocity and tracer fields (1976-2015) to advect numerical particles initialised along
 813 OSNAP East for up to 60 years. We find remarkably close agreement between the structures of
 814 the time-mean Lagrangian overturning within the eastern SPG evaluated in our stationary and
 815 time-evolving fields experiments. However, this similarity masks significant biases introduced
 816 by time-averaging model fields, including the substantial underestimation of northward transport
 817 advected along basin interior pathways within the SPG. Over the duration of our second Lagrangian
 818 experiment, 4.3 Sv of the total 7.2 Sv flowing northwards across the Greenland-Scotland Ridge
 819 returns to OSNAP East via either the dense Nordic seas overflows (3.9 Sv) or the fresh EGCC (0.4
 820 Sv). The remaining 2.9 Sv of cross-ridge transport is partitioned between the net throughflow to
 821 the Arctic Ocean (1.2 Sv) and residual transport (1.7 Sv), representing particles which require more
 822 than 60 years to return to OSNAP East. Crucially, even if all of this residual transport is subducted
 823 into the lower limb of the AMOC along the *IcRo-GSR-Ic/Irm* pathway, the contribution of the
 824 Nordic seas overflows ($3.9 \text{ Sv} + 1.7 \text{ Sv} = 5.6 \text{ Sv}$) would still remain secondary to transformation
 825 within the eastern SPG, albeit closer to the observed estimate of $5.8 \pm 0.7 \text{ Sv}$ (Østerhus et al. 2019).
 826 Although we find that both DSOW and ISOW varieties overturn on multi-decadal timescales, their
 827 final properties are strongly influenced by the excessive entrainment of ambient Atlantic waters
 828 during the several years spent south of the Greenland-Scotland Ridge in this simulation. In contrast
 829 to the substantial overturning variability recorded at OSNAP East (Petit et al. 2020; Desbruyères
 830 et al. 2019; Li et al. 2021), observed overflow transports across the Greenland-Scotland Ridge
 831 exhibit only weak variability on interannual timescales (Østerhus et al. 2019). Thus, while it has
 832 been shown that density anomalies can be imported into the Nordic seas via the Atlantic inflows
 833 (Glessmer et al. 2014; Asbjørnsen et al. 2021), the fact that Lagrangian particles typically integrate
 834 across multiple decades of water mass transformation before returning to OSNAP East means that
 835 anomalous properties are unlikely to persist for long enough to imprint onto overturning variability
 836 via this route.

837 The use of a single eddy-permitting ocean sea-ice hindcast is naturally a limitation of the present
 838 study. While the ORCA025 configuration has been validated extensively within the SPNA region
 839 (e.g., de Boisséson et al. 2010, 2012; Desbruyères et al. 2013, 2015; MacGilchrist et al. 2020, it

840 remains an open question as to how the model's inability to fully resolve ocean turbulence occurring
841 at the mesoscale and submesoscale might impact the faithful representation of the individual
842 overturning pathways comprising the subpolar AMOC. Multi-decadal ocean sea-ice hindcasts are
843 now routinely performed at eddy rich resolutions (at least $1/10^\circ$ according to Hallberg 2013), such
844 as ORCA12 (Marzocchi et al. 2015), FLAME (Böning et al. 2006) and VIKING20 (Biaostoch
845 et al. 2021; Böning et al. 2016), and show substantial improvements in the simulated gyre and
846 overturning circulations compared with observations. In particular, eddy-rich models have been
847 found to more realistically represent the pathways and properties of both the NAC (Marzocchi et al.
848 2015; Breckenfelder et al. 2017) and the Nordic seas overflows south of the Greenland-Scotland
849 Ridge (Behrens et al. 2017). On the other hand, the transition to high resolution models has
850 also introduced new biases, including overestimating the strength of both the subpolar AMOC
851 and SPG circulation when compared with observed estimates (Jackson et al. 2020; Hirschi et al.
852 2020). To complicate this picture, simulated gyre and overturning circulations are also strongly
853 influenced by the surface boundary conditions employed in ocean hindcasts (Biaostoch et al. 2021).
854 Therefore, while it is beyond the scope of this study, addressing the sensitivity of Lagrangian
855 overturning pathways simulated within the SPNA to the choice of both horizontal model resolution
856 and atmospheric forcing remains an important subject in need of further research.

857 This study has demonstrated that the Lagrangian Overturning Function is a valuable addition
858 to existing measures of the density-space overturning (e.g., Marsh 2000; Lozier et al. 2019),
859 owing to its unique ability to connect water mass transformation integrated at the basin-scale to
860 the individual circulation pathways comprising the subpolar AMOC. Extending the Lagrangian
861 overturning framework to investigate how seasonal to multi-decadal overturning variability is
862 manifested amongst the overturning pathways of the SPNA is a logical next step.

863 *Acknowledgments.* O.J. Tooth is grateful for the financial support of the UK Natural Environment
864 Research Council (NE/S007474/1). H.L. Johnson was supported by the NERC-NSF grants SNAP-
865 DRAGON (NE/T013494/1) and WISHBONE (NE/T013451/1). C.W. was supported by the NERC
866 LTS-S CLASS (Climate–Linked Atlantic Sector Science) grant (NE/R015953/1). We would like to
867 thank the European Drakkar project, who carried out the hindcast simulation, and to J. M. Molines
868 and C. Talandier, who kindly provided the data. We additionally thank Laura Jackson, who kindly
869 provided the code to extract the coordinates of OSNAP East array from the ORCA025 model grid.

870 *Data availability statement.* The Lagrangian trajectories used in the analysis can be
871 found at <https://doi.org/10.5281/zenodo.6573900> (Tooth 2022). The Lagrangian trajec-
872 tory code TRACMASS, developed by Aldama-Campino et al. (2020), is available from
873 <https://doi.org/10.5281/zenodo.4337926>. Full details of the NEMO ocean model configura-
874 tion, including access to forcing files, is available on GitHub ([https:// github.com/meom-](https://github.com/meom-configurations/ORCA025.L75-GJM189.git)
875 [configurations/ORCA025.L75-GJM189.git](https://github.com/meom-configurations/ORCA025.L75-GJM189.git)), and has been released with an associated DOI
876 <https://doi.org/10.5281/zenodo.4626012>.

References

- Aldama-Campino, A., K. Döös, J. Kjellsson, and B. Jönsson, 2020: TRACMASS: Formal release of version 7.0 (v7.0-beta). Zenodo. <https://doi.org/10.5281/zenodo.4337926>.
- Asbjørnsen, H., H. L. Johnson, and M. Arthun, 2021: Variable Nordic Seas Inflow Linked to Shifts in North Atlantic Circulation. *Journal of Climate*, **34** (17), 7057–7071, <https://doi.org/10.1175/JCLI-D-20-0917.1>.
- Barnier, B., and Coauthors, 2006: Impact of partial steps and momentum advection schemes in a global ocean circulation model at eddy-permitting resolution. *Ocean Dynamics*, **56** (5-6), 543–567, <https://doi.org/10.1007/s10236-006-0082-1>.
- Behrens, E., K. Våge, B. Harden, A. Biastoch, and C. W. Böning, 2017: Composition and variability of the denmark strait overflow water in a high-resolution numerical model hindcast simulation. *Journal of Geophysical Research: Oceans*, **122** (4), 2830–2846, <https://doi.org/10.1002/2016JC012158>, URL <https://agupubs.onlinelibrary.wiley.com/doi/abs/10.1002/2016JC012158>.
- Bersch, M., J. Meincke, and A. Sy, 1999: Interannual thermohaline changes in the northern North Atlantic 1991-1996. *Deep-Sea Research Part II: Topical Studies in Oceanography*, **46** (1-2), 55–75, [https://doi.org/10.1016/S0967-0645\(98\)00114-3](https://doi.org/10.1016/S0967-0645(98)00114-3).
- Bersch, M., I. Yashayaev, and K. P. Koltermann, 2007: Recent changes of the thermohaline circulation in the subpolar North Atlantic. *Ocean Dynamics*, **57**, 223–235, <https://doi.org/10.1007/s10236-007-0104-7>.
- Biastoch, A., and Coauthors, 2021: Regional imprints of changes in the atlantic meridional overturning circulation in the eddy-rich ocean model viking20x. *Ocean Science*, **17** (5), 1177–1211, <https://doi.org/10.5194/os-17-1177-2021>, URL <https://os.copernicus.org/articles/17/1177/2021/>.
- Biló, T. C., F. Straneo, J. Holte, and I. A. Le Bras, 2022: Arrival of New Great Salinity Anomaly Weakens Convection in the Irminger Sea. *Geophysical Research Letters*, **49** (11), 1–10, <https://doi.org/10.1029/2022GL098857>.

- 904 Blanke, B., and S. Raynaud, 1997: Kinematics of the Pacific Equatorial Undercurrent: An Eulerian
905 and Lagrangian Approach from GCM Results. *Journal of Physical Oceanography*, **27**, 1038–
906 1053, [https://doi.org/10.1175/1520-0485\(1997\)027,1038:KOTPEU.2.0.CO;2](https://doi.org/10.1175/1520-0485(1997)027,1038:KOTPEU.2.0.CO;2).
- 907 Böning, C. W., E. Behrens, A. Biastoch, K. Getzlaff, and J. L. Bamber, 2016: Emerging impact of
908 Greenland meltwater on deepwater formation in the North Atlantic Ocean. *Nature Geoscience*,
909 **9 (7)**, 523–527, <https://doi.org/10.1038/ngeo2740>, URL <https://doi.org/10.1038/ngeo2740>.
- 910 Bower, A., and H. Furey, 2017: Iceland-Scotland Overflow Water transport variability through
911 the Charlie-Gibbs Fracture Zone and the impact of the North Atlantic Current. *Journal of*
912 *Geophysical Research: Oceans*, **122 (9)**, 6989–7012, <https://doi.org/10.1002/2017JC012698>.
- 913 Bower, A., and Coauthors, 2019: Lagrangian Views of the Pathways of the Atlantic Merid-
914 ional Overturning Circulation. *Journal of Geophysical Research: Oceans*, **124 (8)**, 5313–5335,
915 <https://doi.org/10.1029/2019JC015014>.
- 916 Bower, A. S., and Coauthors, 2002: Directly measured mid-depth circulation in the northeastern
917 North Atlantic Ocean. *Nature*, **419 (6907)**, 603–607, <https://doi.org/10.1038/nature01078>.
- 918 Brambilla, E., and L. D. Talley, 2008: Subpolar mode water in the northeastern Atlantic: 1.
919 Averaged properties and mean circulation. *Journal of Geophysical Research: Oceans*, **113 (4)**,
920 1–18, <https://doi.org/10.1029/2006JC004062>.
- 921 Brambilla, E., L. D. Talley, and P. E. Robbins, 2008: Subpolar mode water in the northeastern
922 Atlantic: 2. Origin and transformation. *Journal of Geophysical Research: Oceans*, **113 (4)**,
923 1–16, <https://doi.org/10.1029/2006JC004063>.
- 924 Breckenfelder, T., M. Rhein, A. Roessler, C. W. Böning, A. Biastoch, E. Behrens, and
925 C. Mertens, 2017: Flow paths and variability of the north atlantic current: A com-
926 parison of observations and a high-resolution model. *Journal of Geophysical Research:*
927 *Oceans*, **122 (4)**, 2686–2708, <https://doi.org/https://doi.org/10.1002/2016JC012444>, URL <https://agupubs.onlinelibrary.wiley.com/doi/abs/10.1002/2016JC012444>.
- 928
929 Böning, C. W., M. Scheinert, J. Dengg, A. Biastoch, and A. Funk, 2006: Decadal variability
930 of subpolar gyre transport and its reverberation in the north atlantic overturning. *Geophysical*

Research Letters, **33** (21), <https://doi.org/https://doi.org/10.1029/2006GL026906>, URL <https://agupubs.onlinelibrary.wiley.com/doi/abs/10.1029/2006GL026906>.

Chafik, L., N. P. Holliday, S. Bacon, and T. Rossby, 2022: Irminger sea is the center of action for sub-polar amoc variability. *Geophysical Research Letters*, **49** (17), e2022GL099133, <https://doi.org/https://doi.org/10.1029/2022GL099133>, URL <https://agupubs.onlinelibrary.wiley.com/doi/abs/10.1029/2022GL099133>.

Chafik, L., and T. Rossby, 2019: Volume, Heat, and Freshwater Divergences in the Subpolar North Atlantic Suggest the Nordic Seas as Key to the State of the Meridional Overturning Circulation. *Geophysical Research Letters*, **46** (9), 4799–4808, <https://doi.org/10.1029/2019GL082110>.

Chafik, L., T. Rossby, and C. Schrum, 2014: On the spatial structure and temporal variability of poleward transport between Scotland and Greenland. *Journal of Geophysical Research: Oceans*, **119**, 3868–3882, <https://doi.org/10.1002/2013JC009287>.Received, URL <http://onlinelibrary.wiley.com/doi/10.1002/jgrc.20353/abstract>.

Danabasoglu, G., W. G. Large, and B. P. Briegleb, 2010: Climate impacts of parameterized Nordic Sea overflows. *Journal of Geophysical Research: Oceans*, **115** (11), 1–29, <https://doi.org/10.1029/2010JC006243>.

Danabasoglu, G., and Coauthors, 2014: North Atlantic simulations in Coordinated Ocean-ice Reference Experiments phase II (CORE-II). Part I: Mean states. *Ocean Modelling*, **73**, 76–107, <https://doi.org/10.1016/j.ocemod.2013.10.005>, URL <http://dx.doi.org/10.1016/j.ocemod.2013.10.005>.

Daniault, N., and Coauthors, 2016: The northern North Atlantic Ocean mean circulation in the early 21st century. *Progress in Oceanography*, **146**, 142–158, <https://doi.org/10.1016/j.pocean.2016.06.007>, URL <http://dx.doi.org/10.1016/j.pocean.2016.06.007>.

de Boissésou, E., V. Thierry, H. Mercier, and G. Caniaux, 2010: Mixed layer heat budget in the Iceland Basin from Argo. *Journal of Geophysical Research: Oceans*, **115** (10), 1–15, <https://doi.org/10.1029/2010JC006283>.

- 957 de Boissésou, E., V. Thierry, H. Mercier, G. Caniaux, and D. Desbruyères, 2012: Origin, formation
958 and variability of the Subpolar Mode Water located over the Reykjanes Ridge. *Journal of*
959 *Geophysical Research: Oceans*, **117**, <https://doi.org/10.1029/2011jc007519>.
- 960 de Jong, M. F., L. de Steur, N. Fried, R. Bol, and S. Kritsotakis, 2020: Year-round measurements
961 of the Irminger current: Variability of a two-core current system observed in 2014–2016.
962 *Journal of Geophysical Research: Oceans*, **125** (10), e2020JC016193, [https://doi.org/](https://doi.org/10.1029/2020JC016193)
963 <https://doi.org/10.1029/2020JC016193>, URL [https://agupubs.onlinelibrary.wiley.com/doi/abs/](https://agupubs.onlinelibrary.wiley.com/doi/abs/10.1029/2020JC016193)
964 [10.1029/2020JC016193](https://doi.org/10.1029/2020JC016193).
- 965 de Jong, M. F., H. M. Van Aken, K. Våge, and R. S. Pickart, 2012: Convective mixing in the
966 central Irminger Sea: 2002–2010. *Deep-Sea Research Part I: Oceanographic Research Papers*,
967 **63**, 36–51, <https://doi.org/10.1016/j.dsr.2012.01.003>.
- 968 Dee, D. P., and Coauthors, 2011: The ERA-Interim reanalysis: Configuration and performance of
969 the data assimilation system. *Quarterly Journal of the Royal Meteorological Society*, **137** (656),
970 553–597, <https://doi.org/10.1002/qj.828>.
- 971 Desbruyères, D., L. Chafik, and G. Maze, 2021: A shift in the ocean circulation has warmed
972 the subpolar North Atlantic Ocean since 2016. *Communications Earth & Environment*, **2** (1),
973 <https://doi.org/10.1038/s43247-021-00120-y>.
- 974 Desbruyères, D., H. Mercier, and V. Thierry, 2015: On the mechanisms behind decadal heat content
975 changes in the eastern subpolar gyre. *Progress in Oceanography*, **132**, 262–272, [https://doi.org/](https://doi.org/10.1016/j.pocean.2014.02.005)
976 [10.1016/j.pocean.2014.02.005](https://doi.org/10.1016/j.pocean.2014.02.005).
- 977 Desbruyères, D., V. Thierry, and H. Mercier, 2013: Simulated decadal variability of the meridional
978 overturning circulation across the A25–Ovide section. *Journal of Geophysical Research: Oceans*,
979 **118** (1), 462–475, <https://doi.org/10.1029/2012JC008342>.
- 980 Desbruyères, D. G., H. Mercier, G. Maze, and N. Danialt, 2019: Surface predictor of overturning
981 circulation and heat content change in the subpolar North Atlantic. *Ocean Science*, **15** (3),
982 809–817, <https://doi.org/10.5194/os-15-809-2019>.

- 983 Devana, M. S., W. E. Johns, A. Houk, and S. Zou, 2021: Rapid Freshening of Iceland Scotland
984 Overflow Water Driven By Entrainment of a Major Upper Ocean Salinity Anomaly. *Geophysical*
985 *Research Letters*, 1–11, <https://doi.org/10.1029/2021gl094396>.
- 986 Dickson, B., I. Yashayaev, J. Meincke, B. Turrell, S. Dye, and J. Holfort, 2002: Rapid freshening of
987 the deep North Atlantic Ocean over the past four decades. *Nature*, **416**, 832–837, [https://doi.org/](https://doi.org/10.1038/416832a)
988 [10.1038/416832a](https://doi.org/10.1038/416832a).
- 989 Dickson, B., and Coauthors, 2008: *The Overflow Flux West of Iceland: Variability,*
990 *Origins and Forcing*, 443–474. Springer Netherlands, Dordrecht, [https://doi.org/10.1007/](https://doi.org/10.1007/978-1-4020-6774-7_20)
991 [978-1-4020-6774-7_20](https://doi.org/10.1007/978-1-4020-6774-7_20).
- 992 Dickson, R. R., and J. Brown, 1994: The production of North Atlantic Deep Water: sources, rates,
993 and pathways. *Journal of Geophysical Research*, **99 (C6)**, <https://doi.org/10.1029/94jc00530>.
- 994 Döös, K., 1995: Interocean exchange of water masses. *Journal of Geophysical Research*, **100 (C7)**,
995 499–514, <https://doi.org/10.1029/95jc00337>.
- 996 Döös, K., B. Jönsson, and J. Kjellsson, 2017: Evaluation of oceanic and atmospheric trajectory
997 schemes in the TRACMASS trajectory model v6.0. *Geoscientific Model Development*, **10 (4)**,
998 1733–1749, <https://doi.org/10.5194/gmd-10-1733-2017>.
- 999 Drijfhout, S. S., P. de Vries, K. Döös, and A. C. Coward, 2003: Impact of eddy-induced transport on
1000 the Lagrangian structure of the Upper Branch of the thermohaline circulation. *Journal of Phys-*
1001 *ical Oceanography*, **33 (10)**, 2141–2155, [https://doi.org/10.1175/1520-0485\(2003\)033<2141:](https://doi.org/10.1175/1520-0485(2003)033<2141:IOETOT>2.0.CO;2)
1002 [IOETOT>2.0.CO;2](https://doi.org/10.1175/1520-0485(2003)033<2141:IOETOT>2.0.CO;2).
- 1003 Dussin, R., B. Barnier, L. Brodeau, and J. M. Molines, 2016: The making of the DRAKKAR forcing
1004 set DFS5. Tech. rep., 34 pp. URL [https://www.drakkar-ocean.eu/publications/reports/report{_}](https://www.drakkar-ocean.eu/publications/reports/report{_}DFS5v3{_}April2016.pdf)
1005 [_}DFS5v3{_}April2016.pdf](https://www.drakkar-ocean.eu/publications/reports/report{_}DFS5v3{_}April2016.pdf).
- 1006 Fichet, T., and M. A. Morales Maqueda, 1999: Modelling the influence of snow accumulation
1007 and snow-ice formation on the seasonal cycle of the Antarctic sea-ice cover. *Climate Dynamics*,
1008 **15 (4)**, 251–268, <https://doi.org/10.1007/s003820050280>.

- 1009 Fofonoff, N. P., and R. C. Millard, 1983: Algorithms for computation of fundamental proper-
1010 ties of seawater. *UNESCO Technical papers in marine science*, **44**, 53, URL <http://darchive.mblwhoilibrary.org:8080/handle/1912/2470,j.1365-2486.2005.001000.x>.
1011
- 1012 Foukal, N. P., and M. S. Lozier, 2018: Examining the Origins of Ocean Heat Content Variability
1013 in the Eastern North Atlantic Subpolar Gyre. *Geophysical Research Letters*, **45** (20), 11,275–
1014 11,283, <https://doi.org/10.1029/2018GL079122>.
- 1015 Gary, S. F., M. Susan Lozier, C. W. Böning, and A. Biastoch, 2011: Deciphering the pathways
1016 for the deep limb of the meridional overturning circulation. *Deep Sea Research Part II: Topical
1017 Studies in Oceanography*, **58** (17), 1781–1797, <https://doi.org/https://doi.org/10.1016/j.dsr2.2010.10.059>, URL <https://www.sciencedirect.com/science/article/pii/S0967064511000221>.
1018
- 1019 Georgiou, S., S. L. Ypma, N. Brüggemann, J. Sayol, C. G. van der Boog, P. Spence, J. D. Pietrzak,
1020 and C. A. Katsman, 2021: Direct and Indirect Pathways of Convected Water Masses and Their
1021 impacts on the Overturning Dynamics of the Labrador Sea. *Journal of Geophysical Research:
1022 Oceans*, **126** (1), 1–19, <https://doi.org/10.1029/2020jc016654>.
- 1023 Georgiou, S., S. L. Ypma, N. Brüggemann, J. M. Sayol, J. D. Pietrzak, and C. A. Katsman, 2020:
1024 Pathways of the water masses exiting the Labrador Sea: The importance of boundary–interior
1025 exchanges. *Ocean Modelling*, **150**, 101 623, <https://doi.org/10.1016/j.ocemod.2020.101623>.
- 1026 Glessmer, M. S., T. Eldevik, K. Våge, J. E. Øie Nilsen, and E. Behrens, 2014: Atlantic origin of
1027 observed and modelled freshwater anomalies in the Nordic Seas. *Nature Geoscience*, **7** (11),
1028 801–805, <https://doi.org/10.1038/ngeo2259>.
- 1029 Grist, J. P., S. A. Josey, Z. L. Jacobs, R. Marsh, B. Sinha, and E. Van Sebille, 2016: Ex-
1030 treme air–sea interaction over the North Atlantic subpolar gyre during the winter of 2013–2014
1031 and its sub-surface legacy. *Climate Dynamics*, **46** (11-12), 4027–4045, <https://doi.org/10.1007/s00382-015-2819-3>.
1032
- 1033 Grist, J. P., R. Marsh, and S. A. Josey, 2009: On the relationship between the north Atlantic
1034 meridional overturning circulation and the surface-forced overturning streamfunction. *Journal
1035 of Climate*, **22** (19), 4989–5002, <https://doi.org/10.1175/2009JCLI2574.1>.

- Hallberg, R., 2013: Using a resolution function to regulate parameterizations of oceanic mesoscale eddy effects. *Ocean Modelling*, **72**, 92–103, <https://doi.org/https://doi.org/10.1016/j.ocemod.2013.08.007>, URL <https://www.sciencedirect.com/science/article/pii/S1463500313001601>.
- Hátún, H., A. B. Sande, H. Drange, B. Hansen, and H. Valdimarsson, 2005: Ocean science: Influence of the atlantic subpolar gyre on the thermohaline circulation. *Science*, **309** (5742), 1841–1844, <https://doi.org/10.1126/science.1114777>.
- Hirschi, J. J.-M., and Coauthors, 2020: The atlantic meridional overturning circulation in high-resolution models. *Journal of Geophysical Research: Oceans*, **125** (4), e2019JC015 522, <https://doi.org/https://doi.org/10.1029/2019JC015522>.
- Holliday, N. P., 2003: Air-sea interaction and circulation changes in the northeast Atlantic. *Journal of Geophysical Research: Oceans*, **108** (8), 1–11, <https://doi.org/10.1029/2002jc001344>.
- Holliday, N. P., S. Bacon, J. Allen, and E. L. McDonagh, 2009: Circulation and transport in the western boundary currents at Cape Farewell, Greenland. *Journal of Physical Oceanography*, **39** (8), 1854–1870, <https://doi.org/10.1175/2009JPO4160.1>.
- Holliday, N. P., and Coauthors, 2020: Ocean circulation causes the largest freshening event for 120 years in eastern subpolar North Atlantic. *Nature Communications*, **11**, <https://doi.org/10.1038/s41467-020-14474-y>.
- Houpert, L., S. Cunningham, N. Fraser, C. Johnson, N. P. Holliday, S. Jones, B. Moat, and D. Rayner, 2020: Observed variability of the north atlantic current in the rockall trough from 4 years of mooring measurements. *Journal of Geophysical Research: Oceans*, **125** (10), e2020JC016 403, <https://doi.org/https://doi.org/10.1029/2020JC016403>.
- Houpert, L., M. E. Inall, E. Dumont, S. Gary, C. Johnson, M. Porter, W. E. Johns, and S. A. Cunningham, 2018: Structure and Transport of the North Atlantic Current in the Eastern Subpolar Gyre From Sustained Glider Observations. *Journal of Geophysical Research: Oceans*, **123** (8), 6019–6038, <https://doi.org/10.1029/2018JC014162>.
- Hurrell, J., 1995: Decadal Trends in the North Atlantic Oscillation: Regional Temperatures and Precipitation. *Science*, **269** (5224), 676–679, <https://doi.org/10.1126/science.269.5224.676>.

- 1063 Jackson, L. C., R. Kahana, T. Graham, M. A. Ringer, T. Woollings, J. V. Mecking, and R. A. Wood,
1064 2015: Global and European climate impacts of a slowdown of the AMOC in a high resolution
1065 GCM. *Climate Dynamics*, **45** (11-12), 3299–3316, <https://doi.org/10.1007/s00382-015-2540-2>.
- 1066 Jackson, L. C., and Coauthors, 2020: Impact of ocean resolution and mean state on the
1067 rate of AMOC weakening. *Climate Dynamics*, **55** (7), 1711–1732, <https://doi.org/10.1007/s00382-020-05345-9>.
1068
- 1069 Jochumsen, K., D. Quadfasel, H. Valdimarsson, and S. Jónsson, 2012: Variability of the denmark
1070 strait overflow: Moored time series from 1996–2011. *Journal of Geophysical Research: Oceans*,
1071 **117** (C12), <https://doi.org/https://doi.org/10.1029/2012JC008244>.
- 1072 Johns, W. E., M. Devana, A. Houk, and S. Zou, 2021: Moored Observations of the Iceland-Scotland
1073 Overflow Plume Along the Eastern Flank of the Reykjanes Ridge. *Journal of Geophysical
1074 Research: Oceans*, **126** (8), 1–26, <https://doi.org/10.1029/2021JC017524>.
- 1075 Jones, B. T., A. Solow, and R. Ji, 2016: Resource allocation for lagrangian tracking. *Jour-
1076 nal of Atmospheric and Oceanic Technology*, **33** (6), 1225–1235, [https://doi.org/10.1175/
1077 JTECH-D-15-0115.1](https://doi.org/10.1175/JTECH-D-15-0115.1).
- 1078 Jónsson, S., and H. Valdimarsson, 2005: The flow of Atlantic water to the North Icelandic Shelf
1079 and its relation to the drift of cod larvae. *ICES Journal of Marine Science*, **62** (7), 1350–1359,
1080 <https://doi.org/10.1016/j.icesjms.2005.05.003>.
- 1081 Koman, G., W. E. Johns, and A. Houk, 2020: Transport and evolution of the east reykjanes ridge
1082 current. *Journal of Geophysical Research: Oceans*, **125** (10), e2020JC016377, [https://doi.org/
1083 https://doi.org/10.1029/2020JC016377](https://doi.org/https://doi.org/10.1029/2020JC016377).
- 1084 Lankhorst, M., and W. Zenk, 2006: Lagrangian observations of the middepth and deep velocity
1085 fields of the northeastern Atlantic Ocean. *Journal of Physical Oceanography*, **36** (1), 43–63,
1086 <https://doi.org/10.1175/JPO2869.1>.
- 1087 Large, W. G., J. C. McWilliams, and S. C. Doney, 1994: Oceanic vertical mixing: A review
1088 and a model with a nonlocal boundary layer parameterization. *Reviews of Geophysics*, **32** (4),
1089 363–403, <https://doi.org/10.1029/94RG01872>.

- 1090 Lavender, K. L., R. E. Davis, and W. B. Owens, 2000: Mid-depth recirculation observed in the
1091 interior Labrador and Irminger seas by direct velocity measurements. *Nature*, **407** (6800), 66–69,
1092 <https://doi.org/10.1038/35024048>.
- 1093 Le Bras, I. A., F. Straneo, J. Holte, M. F. de Jong, and N. P. Holliday, 2020: Rapid Export of
1094 Waters Formed by Convection Near the Irminger Sea’s Western Boundary. *Geophysical Research*
1095 *Letters*, **47** (3), <https://doi.org/10.1029/2019GL085989>.
- 1096 Levitus, S., and Coauthors, 1998: World Ocean Database 1998. Tech. rep.
- 1097 Lherminier, P., H. Mercier, C. Gourcuff, M. Alvarez, S. Bacon, and C. Kermabon, 2007: Trans-
1098 ports across the 2002 Greenland-Portugal Ovide section and comparison with 1997. *Journal of*
1099 *Geophysical Research: Oceans*, **112** (7), 1–20, <https://doi.org/10.1029/2006JC003716>.
- 1100 Li, F., and M. S. Lozier, 2018: On the linkage between Labrador Sea Water volume and overturning
1101 circulation in the Labrador Sea: A case study on proxies. *Journal of Climate*, **31** (13), 5225–5241,
1102 <https://doi.org/10.1175/JCLI-D-17-0692.1>.
- 1103 Li, F., M. S. Lozier, and W. E. Johns, 2017: Calculating the meridional volume, heat, and freshwater
1104 transports from an observing system in the subpolar North Atlantic: Observing system simulation
1105 experiment. *Journal of Atmospheric and Oceanic Technology*, **34**, 1483–1500, <https://doi.org/10.1175/JTECH-D-16-0247.1>.
- 1107 Li, F., and Coauthors, 2021: Subpolar North Atlantic western boundary density anomalies and
1108 the Meridional Overturning Circulation. *Nature Communications*, **12** (1), 1–9, <https://doi.org/10.1038/s41467-021-23350-2>.
- 1110 Lozier, M., S. Leadbetter, R. Williams, V. Roussenov, M. Reed, and N. Moore, 2008: The Spatial
1111 Pattern and Mechanisms of Heat-Content Change in the North Atlantic. *Science*, **319** (5864),
1112 800–803, <https://doi.org/10.1126/science.1146436>.
- 1113 Lozier, M. S., and Coauthors, 2017: Overturning in the Subpolar north Atlantic program: A new
1114 international ocean observing system. *Bulletin of the American Meteorological Society*, **98** (4),
1115 737–752, <https://doi.org/10.1175/BAMS-D-16-0057.1>.
- 1116 Lozier, M. S., and Coauthors, 2019: A sea change in our view of overturning in the subpolar North
1117 Atlantic. *Science*, **363** (6426), 516–521, <https://doi.org/10.1126/science.aau6592>.

MacGilchrist, G. A., H. L. Johnson, D. P. Marshall, C. Lique, M. Thomas, L. C. Jackson, and R. A. Wood, 2020: Locations and mechanisms of ocean ventilation in the high-latitude north atlantic in an eddy-permitting ocean model. *Journal of Climate*, **33** (23), 10 113–10 131, <https://doi.org/10.1175/JCLI-D-20-0191.1>.

Madec, G., 2014: NEMO Ocean Engine. Note du Pôle Modélisation de l’Institut Pierre-Simon Laplace 27. Tech. rep.

Marsh, R., 2000: Recent variability of the North Atlantic thermohaline circulation inferred from surface heat and freshwater fluxes. *Journal of Climate*, **13** (18), 3239–3260, [https://doi.org/10.1175/1520-0442\(2000\)013<3239:RVOTNA>2.0.CO;2](https://doi.org/10.1175/1520-0442(2000)013<3239:RVOTNA>2.0.CO;2).

Marzocchi, A., J. J.-M. Hirschi, N. P. Holliday, S. A. Cunningham, A. T. Blaker, and A. C. Coward, 2015: The north atlantic subpolar circulation in an eddy-resolving global ocean model. *Journal of Marine Systems*, **142**, 126–143, <https://doi.org/https://doi.org/10.1016/j.jmarsys.2014.10.007>.

McCarthy, G. D., I. D. Haigh, J. J. Hirschi, J. P. Grist, and D. A. Smeed, 2015: Ocean impact on decadal Atlantic climate variability revealed by sea-level observations. *Nature*, **521** (7553), 508–510, <https://doi.org/10.1038/nature14491>.

McCartney, M. S., and L. D. Talley, 1982: The Subpolar Mode Water of the North Atlantic Ocean. *Journal of Physical Oceanography*, **12**, 1169–1188.

Menary, M. B., D. L. Hodson, J. I. Robson, R. T. Sutton, R. A. Wood, and J. A. Hunt, 2015: Exploring the impact of CMIP5 model biases on the simulation of North Atlantic decadal variability. *Geophysical Research Letters*, **42** (14), 5926–5934, <https://doi.org/10.1002/2015GL064360>.

Menary, M. B., L. C. Jackson, and M. S. Lozier, 2020: Reconciling the Relationship Between the AMOC and Labrador Sea in OSNAP Observations and Climate Models. *Geophysical Research Letters*, **47** (18), <https://doi.org/10.1029/2020GL089793>.

Mercier, H., and Coauthors, 2015: Variability of the meridional overturning circulation at the Greenland-Portugal OVIDE section from 1993 to 2010. *Progress in Oceanography*, **132**, 250–261, <https://doi.org/10.1016/j.pocean.2013.11.001>.

Molines, J.-M., 2021: meom-configurations/ORCA025.L75-GJM189 (V-1.1). Zenodo. <https://doi.org/10.5281/zenodo.4626012>.

1146 Østerhus, S., T. Sherwin, D. Quadfasel, and B. Hansen, 2008: The Overflow Transport East
 1147 of Iceland. *Arctic–Subarctic Ocean Fluxes*, R. P. Dickson R.R., Meincke J., Ed., Springer,
 1148 Dordrecht., 427–441, https://doi.org/https://doi.org/10.1007/978-1-4020-6774-7_19.

1149 Østerhus, S., and Coauthors, 2019: Arctic Mediterranean exchanges: A consistent volume budget
 1150 and trends in transports from two decades of observations. *Ocean Science*, **15** (2), 379–399,
 1151 <https://doi.org/10.5194/os-15-379-2019>.

1152 Paris, C. B., J. Helgers, E. van Sebille, and A. Srinivasan, 2013: Connectivity modeling system:
 1153 A probabilistic modeling tool for the multi-scale tracking of biotic and abiotic variability in the
 1154 ocean. *Environmental Modelling & Software*, **42**, 47–54, [https://doi.org/https://doi.org/10.1016/](https://doi.org/https://doi.org/10.1016/j.envsoft.2012.12.006)
 1155 [j.envsoft.2012.12.006](https://doi.org/https://doi.org/10.1016/j.envsoft.2012.12.006).

1156 Petit, T., M. S. Lozier, S. A. Josey, and S. A. Cunningham, 2020: Atlantic Deep Water Formation
 1157 Occurs Primarily in the Iceland Basin and Irminger Sea by Local Buoyancy Forcing. *Geophysical*
 1158 *Research Letters*, **47** (22), <https://doi.org/10.1029/2020GL091028>.

1159 Petit, T., M. S. Lozier, S. A. Josey, and S. A. Cunningham, 2021: Role of air-sea fluxes and
 1160 ocean surface density on the production of deep waters in the eastern subpolar gyre of the North
 1161 Atlantic. *Ocean Science*, **17**, 1353–1365.

1162 Petit, T., H. Mercier, and V. Thierry, 2018: First Direct Estimates of Volume and Water Mass
 1163 Transports Across the Reykjanes Ridge. *Journal of Geophysical Research: Oceans*, **123** (9),
 1164 6703–6719, <https://doi.org/10.1029/2018JC013999>.

1165 Pickart, R. S., F. Straneo, and G. W. Moore, 2003: Is Labrador Sea Water formed in the
 1166 Irminger basin? *Deep-Sea Research Part I: Oceanographic Research Papers*, **50** (1), 23–52,
 1167 [https://doi.org/10.1016/S0967-0637\(02\)00134-6](https://doi.org/10.1016/S0967-0637(02)00134-6).

1168 Piron, A., V. Thierry, H. Mercier, and G. Caniaux, 2016: Argo float observations of basin-scale
 1169 deep convection in the Irminger sea during winter 2011–2012. *Deep-Sea Research Part I:*
 1170 *Oceanographic Research Papers*, **109**, 76–90, <https://doi.org/10.1016/j.dsr.2015.12.012>.

1171 Read, J. F., 2000: CONVEX-91: Water masses and circulation of the Northeast Atlantic subpo-
 1172 lar gyre. *Progress in Oceanography*, **48** (4), 461–510, [https://doi.org/10.1016/S0079-6611\(01\)](https://doi.org/10.1016/S0079-6611(01)00011-8)
 1173 [00011-8](https://doi.org/10.1016/S0079-6611(01)00011-8).

- 1174 Roberts, M., R. Wood, R. Marsh, and A. New, 1996: An Intercomparison of a Bryan–Cox-
1175 Type Ocean Model and an Isopycnic Ocean Model. Part I: The Subpolar Gyre and High-
1176 Latitude Processes. *Journal of Physical Oceanography*, **26**, 1495–1527, [https://doi.org/10.1175/
1177 1520-0485\(1996\)026<1495:AIOABT>2.0.CO;2](https://doi.org/10.1175/1520-0485(1996)026<1495:AIOABT>2.0.CO;2).
- 1178 Roussenov, V. M., R. G. Williams, M. S. Lozier, N. P. Holliday, and D. M. Smith, 2022: Historical
1179 reconstruction of subpolar north atlantic overturning and its relationship to density. *Journal
1180 of Geophysical Research: Oceans*, **127** (6), e2021JC017732, [https://doi.org/https://doi.org/10.
1181 1029/2021JC017732](https://doi.org/https://doi.org/10.1029/2021JC017732).
- 1182 Sarafanov, A., 2009: On the effect of the north Atlantic oscillation on temperature and salinity
1183 of the subpolar north Atlantic intermediate and deep waters. *ICES Journal of Marine Science*,
1184 **66** (7), 1448–1454, <https://doi.org/10.1093/icesjms/fsp094>.
- 1185 Sarafanov, A., H. Mercier, A. Falina, A. Sokov, and P. Lherminier, 2010: Cessation and partial
1186 reversal of deep water freshening in the northern North Atlantic: Observation-based estimates
1187 and attribution. *Tellus, Series A: Dynamic Meteorology and Oceanography*, **62** (1), 80–90,
1188 <https://doi.org/10.1111/j.1600-0870.2009.00418.x>.
- 1189 Sarafanov, A., and Coauthors, 2012: Mean full-depth summer circulation and transports at the
1190 northern periphery of the Atlantic Ocean in the 2000s. *Journal of Geophysical Research: Oceans*,
1191 **117** (1), 1–22, <https://doi.org/10.1029/2011JC007572>.
- 1192 Steele, M., R. Morley, and W. Ermold, 2001: PHC: a global hydrography with a high quality Arctic
1193 Ocean. *Journal of Climate*, **14** (9), 2079–2087, URL <https://www.jstor.org/stable/26247422>.
- 1194 Stöven, T., T. Tanhua, M. Hoppema, and W.-J. von Appen, 2016: Transient tracer distributions in
1195 the fram strait in 2012 and inferred anthropogenic carbon content and transport. *Ocean Science*,
1196 **12** (1), 319–333, <https://doi.org/10.5194/os-12-319-2016>.
- 1197 Thierry, V., E. de Boisséon, and H. Mercier, 2008: Interannual variability of the Subpolar Mode
1198 Water properties over the Reykjanes Ridge during 1990–2006. *Journal of Geophysical Research:
1199 Oceans*, **113** (4), 1–14, <https://doi.org/10.1029/2007JC004443>.
- 1200 Tooth, O., 2022: Lagrangian overturning in the eastern subpolar North Atlantic - ORCA025-
1201 GJM189 Particle Trajectory Dataset. Zenodo. <https://doi.org/10.5281/zenodo.6573900>.

- Uppala, S. M., and Coauthors, 2005: The ERA-40 re-analysis. *Quarterly Journal of the Royal Meteorological Society*, **131** (612), 2961–3012, <https://doi.org/10.1256/qj.04.176>.
- Våge, K., and Coauthors, 2011: The Irminger Gyre: Circulation, convection, and interannual variability. *Deep-Sea Research Part I: Oceanographic Research Papers*, **58** (5), 590–614, <https://doi.org/10.1016/j.dsr.2011.03.001>.
- Van Aken, H. M., and C. J. De Boer, 1995: On the synoptic hydrography of intermediate and deep water masses in the Iceland Basin. *Deep-Sea Research Part I*, **42** (2), 165–189, [https://doi.org/10.1016/0967-0637\(94\)00042-Q](https://doi.org/10.1016/0967-0637(94)00042-Q).
- Van Sebille, E., P. Spence, M. R. Mazloff, M. H. England, S. R. Rintoul, and O. A. Saenko, 2013: Abyssal connections of Antarctic Bottom Water in a Southern Ocean State Estimate. *Geophysical Research Letters*, **40** (10), 2177–2182, <https://doi.org/10.1002/grl.50483>.
- Wang, H., S. A. Legg, and R. W. Hallberg, 2015: Representations of the Nordic Seas overflows and their large scale climate impact in coupled models. *Ocean Modelling*, **86**, 76–92, <https://doi.org/10.1016/j.ocemod.2014.12.005>.
- Waterhouse, A. F., and Coauthors, 2014: Global patterns of diapycnal mixing from measurements of the turbulent dissipation rate. *Journal of Physical Oceanography*, **44** (7), 1854–1872, <https://doi.org/10.1175/JPO-D-13-0104.1>.
- Wefing, A.-M., N. Casacuberta, M. Christl, N. Gruber, and J. N. Smith, 2021: Circulation timescales of atlantic water in the arctic ocean determined from anthropogenic radionuclides. *Ocean Science*, **17** (1), 111–129, <https://doi.org/10.5194/os-17-111-2021>.
- Winton, M., R. Hallberg, and A. Gnanadesikan, 1998: Simulation of density-driven frictional downslope flow in Z-coordinate ocean models. *Journal of Physical Oceanography*, **28** (11), 2163–2174, [https://doi.org/10.1175/1520-0485\(1998\)028<2163:SODDFD>2.0.CO;2](https://doi.org/10.1175/1520-0485(1998)028<2163:SODDFD>2.0.CO;2).
- Xu, X., P. B. Rhines, and E. P. Chassignet, 2016: Temperature–salinity structure of the north atlantic circulation and associated heat and freshwater transports. *Journal of Climate*, **29** (21), 7723 – 7742, <https://doi.org/10.1175/JCLI-D-15-0798.1>.
- Xu, X., W. J. Schmitz, H. E. Hurlburt, P. J. Hogan, and E. P. Chassignet, 2010: Transport of Nordic Seas overflow water into and within the Irminger Sea: An eddy-resolving simulation

and observations. *Journal of Geophysical Research: Oceans*, **115** (12), 1–20, <https://doi.org/10.1029/2010JC006351>.

Yashayaev, I., and R. Dickson, 2008: Transformation and fate of overflows in the Northern North Atlantic. *Arctic–Subarctic Ocean Fluxes*, R. Dickson, J. Meincke, and P. Rhines, Eds., Springer, Dordrecht., 505–526, https://doi.org/doi:10.1007/978-1-4020-6774-7_22.

Yashayaev, I., and J. W. Loder, 2016: Recurrent replenishment of labrador sea water and associated decadal-scale variability. *Journal of Geophysical Research: Oceans*, **121** (11), 8095–8114, <https://doi.org/https://doi.org/10.1002/2016JC012046>.

Yeager, S. G., A. R. Karspeck, and G. Danabasoglu, 2015: Predicted slowdown in the rate of Atlantic sea ice loss. *Geophysical Research Letters*, **42** (24), 10 704–10 713, <https://doi.org/10.1002/2015GL065364>.

Zhang, R., and M. Thomas, 2021: Horizontal circulation across density surfaces contributes substantially to the long-term mean northern Atlantic Meridional Overturning Circulation. *Communications Earth & Environment*, **2** (1), <https://doi.org/10.1038/s43247-021-00182-y>.

Zou, S., A. Bower, H. Furey, M. Susan Lozier, and X. Xu, 2020a: Redrawing the Iceland-Scotland Overflow Water pathways in the North Atlantic. *Nature Communications*, **11** (1), <https://doi.org/10.1038/s41467-020-15513-4>.

Zou, S., M. S. Lozier, F. Li, R. Abernathey, and L. Jackson, 2020b: Density-compensated overturning in the Labrador Sea. *Nature Geoscience*, **13** (2), 121–126, <https://doi.org/10.1038/s41561-019-0517-1>.